Published January 21, 2008
JEM

BRIEF DEFINITIVE REPORT

Periostin is essential for cardiac healing after acute myocardial infarction

Masashi Shimazaki,[1] Kazuto Nakamura,[2] Isao Kii,[1] Takeshi Kashima,[3] Norio Amizuka,[4] Minqi Li,[4] Mitsuru Saito,[5] Keiichi Fukuda,[6] Takashi Nishiyama,[1] Satoshi Kitajima,[7] Yumiko Saga,[8] Masashi Fukayama,[3] Masataka Sata,[2] and Akira Kudo[1]

[1]Department of Biological Information, Tokyo Institute of Technology, Yokohama 226-8501, Japan
[2]Department of Cardiovascular Medicine and [3]Department of Pathology, Graduate School of Medicine, The University of Tokyo, Tokyo 113-0033, Japan
[4]Center for Transdisciplinary Research, Niigata University, Niigata 951-8514, Japan
[5]Department of Orthopaedic Surgery, Jikei University School of Medicine, Tokyo 105-8461, Japan
[6]Department of Regenerative Medicine and Advanced Cardiac Therapeutics, Keio University School of Medicine, Tokyo 160-8582, Japan
[7]Division of Cellular and Molecular Toxicology, National Institute of Health Science, Tokyo 158-8501, Japan
[8]Division of Mammalian Development, National Institute of Genetics, Mishima 411-8540, Japan

Acute myocardial infarction (AMI) is a common and lethal heart disease, and the recruitment of fibroblastic cells to the infarct region is essential for the cardiac healing process. Although stiffness of the extracellular matrix in the infarct myocardium is associated with cardiac healing, the molecular mechanism of cardiac healing is not fully understood. We show that periostin, which is a matricellular protein, is important for the cardiac healing process after AMI. The expression of periostin protein was abundant in the infarct border of human and mouse hearts with AMI. We generated *periostin*$^{-/-}$ mice and found no morphologically abnormal cardiomyocyte phenotypes; however, after AMI, cardiac healing was impaired in these mice, resulting in cardiac rupture as a consequence of reduced myocardial stiffness caused by a reduced number of α smooth muscle actin–positive cells, impaired collagen fibril formation, and decreased phosphorylation of FAK. These phenotypes were rescued by gene transfer of a spliced form of periostin. Moreover, the inhibition of FAK or αv-integrin, which blocked the periostin-promoted cell migration, revealed that αv-integrin, FAK, and Akt are involved in periostin signaling. Our novel findings show the effects of periostin on recruitment of activated fibroblasts through FAK-integrin signaling and on their collagen fibril formation specific to healing after AMI.

CORRESPONDENCE
Akira Kudo:
akudo@bio.titech.ac.jp

Periostin, which is an extracellular matrix (ECM) molecule of the fasciclin family, acts in cell adhesion, migration, and growth in vitro (1–6). In the heart, periostin is expressed at very early stages of embryogenesis; however, it is not detected in the normal adult myocardium, except in the valves (7, 8) and in the case of various heart diseases (9–12).

The early cardiac healing process after acute myocardial infarction (AMI) can be divided into two successive phases: the inflammatory phase and the scar formation phase. In the inflammatory phase, monocytes and lymphocytes infiltrate into the necrotic myocardium, whereas in the scar formation phase, activated interstitial or circulating fibroblasts increase their motility and migrate into the lesion. The activation of TGFβ is important for regulation of this latter process. Myofibroblasts expressing α smooth muscle actin (αSMA) induced by TGFβ are specialized fibroblasts that share characteristics with smooth muscle cells (SMCs). They play an important role in wound healing by synthesizing ECM and exerting strong contraction forces to minimize wound areas (13–16). Regarding the inflammatory phase, recent knockout mouse studies indicated a positive association of inflammatory factors with cardiac rupture or dilation (17–23). However, in the scar formation phase, molecular analysis has been scant, except in respect to TGFβ. To answer two important questions for both cardiologists and basic scientists who are interested in pathological myocardial healing, i.e., "what regulates formation of

The online version of this article contains supplemental material.

The Journal of Experimental Medicine

Downloaded from jem.rupress.org on June 11, 2009

JEM © The Rockefeller University Press $30.00
Vol. 205, No. 2, February 18, 2008 295-303 www.jem.org/cgi/doi/10.1084/jem.20071297

Supplemental Material can be found at:
http://jem.rupress.org/cgi/content/full/jem.20071297/DC1

the scar phase of an ischemic injury?" and "what is the nature of the factors responsible for the ventricular healing process after AMI?," we focused on periostin, which is a TGFβ-responding factor (1).

RESULTS AND DISCUSSION

To assess the importance of periostin in the cardiac healing process, we examined the expression of human periostin protein in the myocardial tissue of the left ventricle (LV). No expression of it was observed in the normal myocardium (Fig. 1 A), whereas immunoreactivity indicating periostin was detected in Azan-stained myocardial fibrous areas from a patient with AMI (Fig. 1, B and C), thus suggesting that periostin expression was induced in the infarct regions after AMI. In the fibrous area, strong immunoreactivity of periostin was observed around cardiac fibroblasts expressing αv-integrin, which is reported to be a receptor for periostin (Fig. 1 C) (2, 6). Next, we examined the expression of periostin in mice after AMI caused by left anterior descending artery (LAD) ligation (24). Periostin protein was not observed up to day 2, but became detectable at day 3 in the areas showing inflammatory infiltration (Fig. 1 D). This expression in the infarct LV increased significantly at day 4, and was still present at day 28 (Fig. 1 D and not depicted). To identify the cells producing periostin, we performed RNA in situ hybridization to detect *periostin* mRNA in the infarct LV wall of mice. *Periostin* mRNA was mainly expressed in fibroblasts in both the infarct and noninfarct regions after AMI (Fig. 1 E). To confirm the periostin expression in cardiac fibroblasts, we performed RT-PCR analysis on purified cardiac cells, and these results showed the expression to be mainly in cardiac fibroblasts, but not in cardiomyocytes (Fig. S1, available at http://www.jem.org/cgi/content/full/jem.20071297/DC1). Furthermore, these fibroblasts were positive for αv-integrin, as indicated by flow cytometry using cultured cardiac cells (Fig. S1). The mRNA of *βig-h3*, another fasciclin family member, which is also expressed in the embryonic heart (25), was not observed in

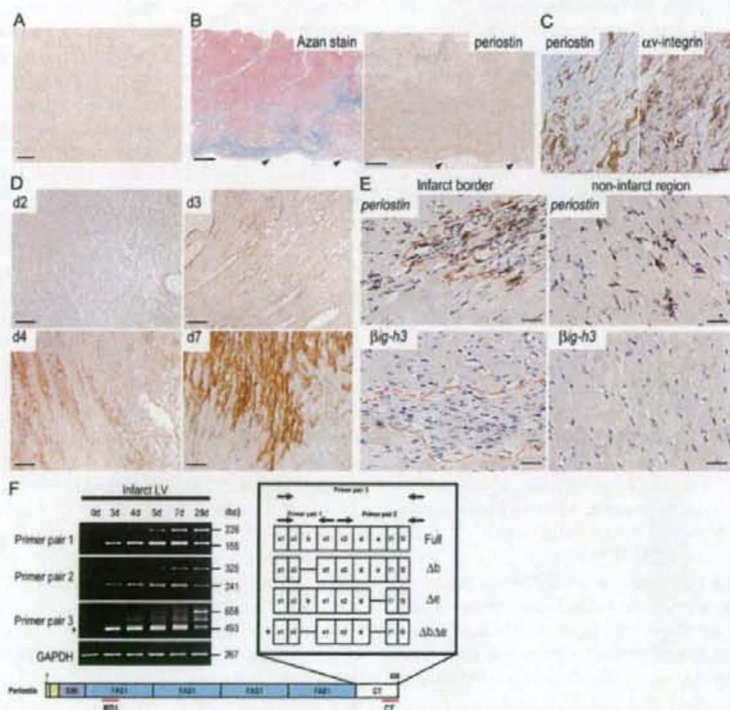

Figure 1. Periostin expression is induced after myocardial ischemia. (A–C) Detection of periostin in myocardium from human patients. LV tissue from a patient with alcoholic cirrhosis (A) and from a patient with AMI (B and C). As seen by immunostaining, periostin protein was detected (B, right) in the myocardial area, which was shown to be fibrous by Azan staining (B, left). Arrowheads in B indicate endocardium. (C) Comparison of the expression pattern between periostin (left) and αv-integrin (right) in the fibrous area. (D–F) Periostin is up-regulated after AMI in mice. (D) Immunostaining of periostin after AMI. (E) Expression of *periostin* (top) and β *ig-h3* mRNA (bottom) in the infarct LV wall of mice was analyzed by in situ hybridization. The dashed red line shows the infarct border. (F) Expression of spliced variant forms of periostin at various times after AMI. Periostin ΔbΔe is indicated by the asterisk. Bars: (A) 25 μm; (B) 2 mm; (C–E) 50 μm.

Downloaded from jem.rupress.org on June 11, 2009

the same regions (Fig. 1 E), thus suggesting the AMI-induced expression of fasciclin family molecules to be specific to periostin.

Because we previously reported that several *periostin* transcripts exist in human and mouse, caused by alternative splicing at a 3′ site (1), we examined the expression of the splice variants in a time course experiment by RT-PCR analysis using three combinations of specific primers (Fig. 1 F). We observed four different isoforms, i.e., Δb (deletion of b domain), Δe (deletion of e domain), ΔbΔe (deletion of b and e domains), and Full (full-length), and we found that the pattern of splicing depended on the time after AMI. Interestingly, one specific spliced form, ΔbΔe (Fig. 1 F, asterisk), was dominantly found as the lowest electrophoretic band in the initial stages (3, 4, and 5 d after AMI), indicating the involvement of ΔbΔe periostin in the early healing stage of damaged tissues. By 28 d, all 4 isoforms were equally expressed. We also confirmed the expression of these isoforms at the protein level, and found the proteolytic modification of periostin during infarct healing (Fig. S1).

To investigate the role of periostin in AMI, we generated *periostin*$^{-/-}$ mice combined with Cre recombination (Fig. 2 A and Fig. S2, available at http://www.jem.org/cgi/content/full/jem.20071297/DC1). The embryogenesis of *periostin*$^{-/-}$ mice was apparently normal; and after the birth, the mice appeared to be healthy. The observation of periostin in the developing heart prompted us to thoroughly investigate the heart structure and function in the *periostin*$^{-/-}$ mice; however, no cardiomyocyte abnormalities were found in the myocardium, valve function, pulsation, or blood pressure in the 10-wk-old mice (Fig. S2 and not depicted), which is consistent with no significant expression in the adult myocardium. We then subjected *periostin*$^{-/-}$ mice to AMI by LAD ligation. There was no significant difference in body weight or heart rate among $^{-/-}$, $^{+/-}$, and $^{+/+}$ in the normal control condition or after the AMI (Fig. S2, Table S1, and not depicted); moreover, there was no difference in infarct size between the *periostin*$^{+/+}$ and $^{-/-}$ mice after AMI (Table S1). However, the survival rate of *periostin*$^{-/-}$ mice after AMI was significantly lower than that of $^{+/+}$ mice (17.58 vs. 53.76% at day 10; $P < 0.0001$; Fig. 2 B), whereas this rate of *periostin*$^{+/-}$ mice (55%) after AMI was similar to that of $^{+/+}$ mice. The incidence of mortality in *periostin*$^{-/-}$ mice, mainly caused by cardiac rupture, which occurred within 7 d, was significantly higher ($P < 0.001$) than that of $^{+/+}$ mice: 62/91 (68.1%) in $^{-/-}$ versus 25/80 (31.3%) in $^{+/+}$ (Fig. 3 C), whereas this frequency of $^{+/-}$ mice 6/20 (30%) was similar to that of $^{+/+}$ mice. Thereafter, these survival rates reached a plateau from 8 d up to 4 wk after AMI (unpublished data). To test whether the increased rate of cardiac rupture was caused by abnormal LV wall stiffness, we analyzed the rupture threshold stiffness of the LVs of *periostin*$^{-/-}$ and $^{+/+}$ mice 4 d after AMI by conducting an LV distending pressure/rupture threshold study (18). Myocardial tearing was found at the infarct border in all the ruptured LVs, and the mean of the maximum rupture pressure was significantly lower in *periostin*$^{-/-}$ mice than in $^{+/+}$ mice after AMI (312.7 ± 3.2 mmHg in $^{-/-}$ vs. 374.3 ± 5.8 mmHg in $^{+/+}$; $P = 0.0008$; $n = 5$), and the mean passive stiffness was also significantly lower in $^{-/-}$ mice than in $^{+/+}$ mice after AMI (50.26 ± 2.13 mmHg/100 μl in $^{-/-}$ vs. 65.08 ± 2.55 mmHg/100 μl in $^{+/+}$; $P = 0.001$; $n = 5$; Fig. 2 C). In contrast, no significant difference was observed between $^{+/+}$ control noninfarct mice and *periostin*$^{-/-}$ control noninfarct mice (maximum rupture pressure was 544.0 ± 6.93 mmHg in $^{-/-}$ vs. 552.7 ± 7.86 mmHg in $^{+/+}$; $P = 0.4546$; $n = 5$; mean passive stiffness was 87.07 ± 4.41 mmHg/100 μl in $^{-/-}$ vs. 88.85 ± 3.14 mmHg/100 μl in $^{+/+}$; $P = 0.5985$; $n = 5$). These biomechanical data indicate that both rupture threshold and passive stiffness in the LV of the *periostin*$^{-/-}$ infarcted mice were significantly lower than those of the $^{+/+}$ mice after AMI, suggesting that the *periostin*$^{-/-}$ infarct LV wall was more susceptible to cardiac rupture by mechanical stress. Although periostin deficiency did not affect heart structure, the circulatory system, or cardiac performance under physiological conditions, periostin induced in the infarct myocardium appears to play a pivotal role in the healing process after AMI.

To confirm the histomorphological stiffness of the wall in *periostin*$^{-/-}$ mice just escaping from rupture, we performed echocardiography 7 d after AMI, in addition to 1 d for heart tissue evaluation and 28 d for the analysis of chronic cardiac pathophysiology after AMI (Fig. 2 D and Table S1). Echocardiographic measurements made 7 d after AMI showed decreases in left ventricular end-diastolic dimension (LVEDD) and left ventricular end-systolic dimension (LVESD) in *periostin*$^{-/-}$ mice ($n = 10$), as compared with these parameters for $^{+/+}$ mice ($n = 15$; LVEDD and LVESD values for $^{-/-}$ were 89.0 and 84.4%, respectively, of those for $^{+/+}$). These results demonstrate that the absence of periostin attenuated ventricular remodeling after AMI. To further examine tissue stiffness histologically, we performed toluidine blue staining, immunofluorescence analysis using anti–collagen I, -fibronectin, and -vimentin antibodies, and transmission electron microscopic (TEM) observation of sections prepared from *periostin*$^{+/+}$ and $^{-/-}$ mice 5 d after AMI. The results showed a lower number of cardiac fibroblasts, along with sparser pericellular ECM density in the *periostin*$^{-/-}$ mice than in the $^{+/+}$ mice (Fig. 2, E and F); indeed, the number of vimentin-positive cardiac fibroblasts was decreased in the infarct region of *periostin*$^{-/-}$ mice 5 d after AMI (7,655 ± 148 cells/mm^2 in $^{+/+}$ vs. 6,913 ± 297 cells/mm^2 in $^{-/-}$; $n = 6$; $P < 0.02$; Fig. 2 C). Furthermore, reduced collagen I and fibronectin immunoreactivity was observed in the infarct border of the $^{-/-}$ mice (Fig. 2 F and Fig. S3, available at http://www.jem.org/cgi/content/full/jem.20071297/DC1), and the collagen fiber cross-sectional area (CSA) in the infarct border of *periostin*$^{-/-}$ mice was significantly smaller and more uniform than that of $^{+/+}$ mice 5 d after AMI (CSA of 1,014.642 ± 17.546 nm^2 for the $^{-/-}$ and 2,233.780 ± 25.731 nm^2 for the $^{+/+}$; $n = 6$; $P < 0.001$, respectively; Fig. 2 G). To confirm whether periostin deficiency affected the biochemical property of collagen after AMI, we evaluated the amount of collagen (hydroxyproline concentration, percentage of tissue dry weight) and nonreducible mature cross-links (mol pyridinoline per mol collagen) in the infarct zone 4 d after AMI. We detected a significant decrease in the collagen cross-linking in the *periostin*$^{-/-}$ mice, compared with the $^{+/+}$ mice

Downloaded from jem.rupress.org on June 11, 2009

Published January 21, 2008

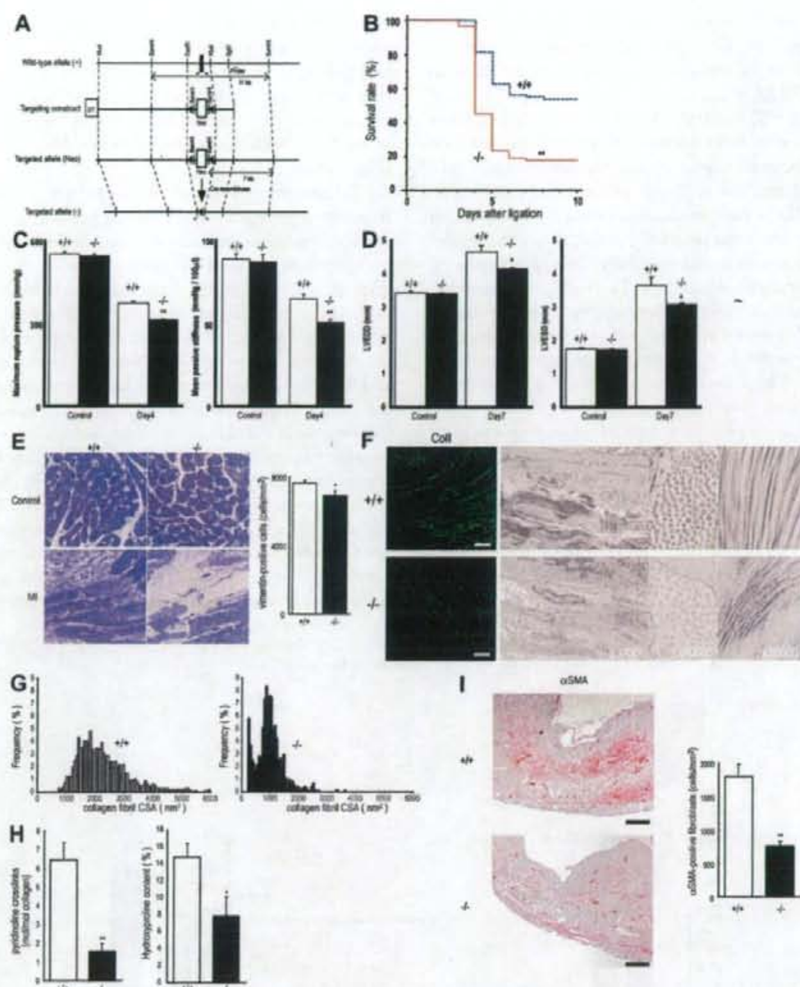

Figure 2. Cardiac rupture after AMI is caused by *periostin* disruption. (A) Schema of the targeting strategy deletes the first exon of *periostin* locus. (B) Decreased survival of *periostin*$^{-/-}$ mice ($n = 91$) compared with the survival of $^{+/+}$ mice ($n = 80$) after AMI. **, $P < 0.0001$. (C) Infarct LV wall stiffness was more reduced in *periostin*$^{-/-}$ mice than in $^{+/+}$ mice after AMI (left). Mean passive stiffness was also significantly lower in the $^{-/-}$ mice than in the $^{+/+}$ mice after AMI (right). Open columns, $^{+/+}$; filled columns, $^{-/-}$. **, $P < 0.005$, compared with $^{+/+}$ mice. (D) Loss of periostin attenuated cardiac dilation after AMI, as shown by echocardiography. Open columns, $^{+/+}$; filled columns, $^{-/-}$. *, $P < 0.05$ compared with $^{+/+}$ mice. (E) Histological analysis of heart sections from *periostin*$^{-/-}$ and $^{+/+}$ mice stained with toluidine blue 5 d after AMI, showing a lower number of cardiac fibroblasts and lower ECM density in $^{-/-}$ mice. (right) The number of vimentin-positive cells. *, $P < 0.02$, compared with $^{+/+}$ mice. (F) Images of the infarct border stained with anti-collagen I (left), and TEM images of infarct border, showing evidence of smaller and less abundant collagen in tissues from *periostin*$^{-/-}$ mice 5 d after AMI compared with the collagen of the $^{+/+}$ infarct heart. Bar, 50 µm. (G) CSA distribution of collagen fibrils in the infarct border of $^{+/+}$ and $^{-/-}$ mice, measured from TEM images. (H) Biochemical analysis of the collagen amount and cross-linking. *, $P < 0.05$; **, $P < 0.01$, compared with $^{+/+}$ mice. (I) The number of αSMA-positive cells in the infarct area was reduced in *periostin*$^{-/-}$ mice 5 d after AMI. (right) The number of αSMA-positive cells. **, $P < 0.01$, compared with $^{+/+}$ mice. Error bars represent the mean ± the SEM. Bars, 200 µm.

Downloaded from jem.rupress.org on June 11, 2009

(1.555 ± 0.461 in $^{-/-}$, $n = 4$, vs. 6.433 ± 0.919 in $^{+/+}$, $n = 7$; $P = 0.0043$; Fig. 2 H). Moreover, the *periostin*$^{-/-}$ infarct LV tissue exhibited 52.9% less collagen content compared with the $^{+/+}$ tissue (7.832 ± 2.241% in $^{-/-}$, $n = 4$, vs. 14.795 ± 1.565% in $^{+/+}$, $n = 7$; $P = 0.0283$; Fig. 2 H). In normal heart tissues from mice of either genotype, the collagen amount was under the detection level by our methods (unpublished data), indicating that the detected collagen was newly produced after AMI. In conclusion, we observed the alterations of collagen structure in the *periostin*$^{-/-}$ mice; they were smaller and more uniform, with the decreased amount and cross-linking of collagen effecting lower stiffness. These results suggest that periostin expression contributed significantly to the amount or cross-linking of newly synthesized collagen, which is essential for the normal mechanical properties of collagen-containing tissues after MI. These findings indicate that impaired collagen fiber formation occurred in *periostin*$^{-/-}$ mice after AMI. Interestingly, although the total activity of myeloperoxidase and the numbers of Mac-3–positive inflammatory cells, ki67-positive proliferating cells, and active caspase-3–positive apoptotic cells in the infarct border were not significantly different between $^{+/+}$ and $^{-/-}$ mice (not depicted), we observed a lower number of αSMA-positive cells in the infarct area of *periostin*$^{-/-}$ mice 5 d after AMI ($1,792 \pm 193$ cells/mm^2 in $^{+/+}$ vs. 758 ± 75 cells/mm^2 in $^{-/-}$; $P < 0.01$; $n = 6$; Fig. 2 I). However, the number of cells positive for SM1, which is a specific marker of SMCs, was not significantly different, and almost all of the αSMA-positive cells were SM1 negative (unpublished data). These results indicate that not the inflammatory cell recruitment, but rather the recruitment of cardiac fibroblasts in the infarct region, was impaired in these animals.

To determine whether the impaired cardiac healing in response to AMI could be restored by periostin directly, we performed a rescue experiment by using ΔbΔe, which is the main periostin isoform detected early after AMI. The *periostin*$^{-/-}$ mice were treated with a recombinant adenovirus expressing periostin (Ad-ΔbΔe) or with a control adenovirus (Ad-nls; nuclear localization signal-LacZ). In the control experiment, the Ad-nls-LacZ transfer was detected in the infarct border at 4 d after AMI by whole-mount X-gal staining, proving the experimental feasibility (Fig. 3 A). In *periostin*$^{-/-}$ mice infected with Ad-ΔbΔe, we first confirmed expression of transferred periostin in the infarct tissue by immunoblot and immunofluorescence analyses (Fig. 3 B and Fig. S4, available at http://www.jem.org/cgi/content/full/jem.20071297/DC1), and then observed an increase in the area reactive with anti-αSMA antibody compared with that area of the control Ad-nls-LacZ–infected *periostin*$^{-/-}$ mice (597 ± 107 cells/mm^2 in Ad-nls-LacZ–infected $^{-/-}$ mice vs. $1,535 \pm 197$ cells/mm^2

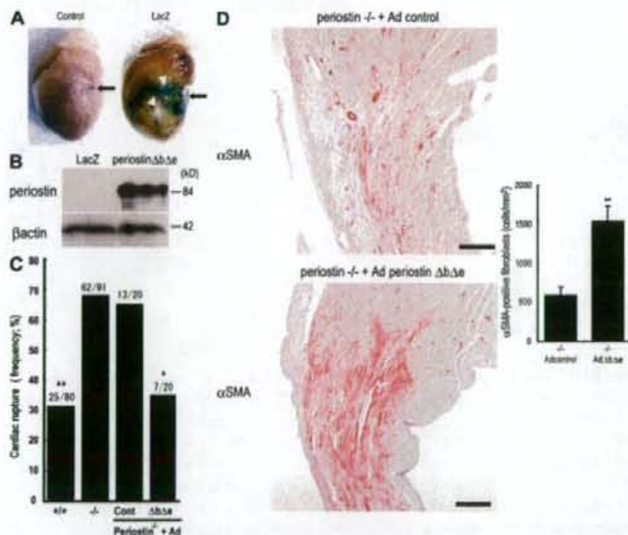

Figure 3. Adenovirus-mediated periostin ΔbΔe gene transfer prevents cardiac rupture in the *periostin*$^{-/-}$ mice. (A) Whole-mount X-gal staining 4 d after AMI showed strong expression in the border of the Ad-nls-LacZ–infected myocardial infarct (arrowheads). The arrow indicates the ligated portion. (B) Western blot analysis for Ad-ΔbΔe–infected *periostin*$^{-/-}$ infarct LV. (C) Infection with Ad-ΔbΔe reversed the high incidence of cardiac rupture in the *periostin*$^{-/-}$ mice to a lower level, comparable to the incidence in the $^{+/+}$ mice. *, $P < 0.02$; **, $P < 0.001$, compared with control Ad-treated $^{-/-}$ mice. (D) Compared with the Ad-nls-LacZ–infected *periostin*$^{-/-}$ hearts, the Ad-ΔbΔe–infected hearts increased the number of αSMA-positive cells 5 d after AMI. (right) the number of αSMA-positive cells. **, $P < 0.01$, compared with the mock infection of the $^{-/-}$ mice. Error bars represent the mean ± the SEM. Bars, 200 μm.

Downloaded from jem.rupress.org on June 11, 2009

Published January 21, 2008

in Ad-ΔbΔe–infected $^{-/-}$ mice; $P < 0.01$; $n = 6$; Fig. 3 D). Furthermore, the Ad-ΔbΔe infection reduced the incidence of rupture frequency in *periostin*$^{-/-}$ mice (35.0%) compared with that for the Ad-nls-LacZ–treated $-/-$ mice (65.0%; Fig. 3 C). These results demonstrate that periostin ΔbΔe was essential for in vivo recruitment of αSMA-positive fibroblasts to block rupture after AMI. As cell motility and morphology of fibroblasts are associated with the expression of the phosphorylated forms of Akt and focal adhesion kinase (FAK) (26, 27), we examined the phosphorylation of these proteins in the infarct border 5 d after AMI. The amount of phosphorylated Akt was reduced, and only a small amount of phosphorylated FAK was detected in the border of the *periostin*$^{-/-}$ infarcted mice (Fig. 4, A and B, and Fig. S5).

To further investigate the role of periostin in FAK activation and cell motility, we performed immunofluorescence staining for phosphorylated-FAK and rhodamine-phalloidin staining for the actin cytoskeleton in an embryonic mesenchymal cell line, C3H10T1/2, treated or not with periostin ΔbΔe. The presence of periostin ΔbΔe changed the cytoskeletal arrangement and motility of the cells, resulting in dynamic protrusion of their processes (Fig. 4 C). In a time-course

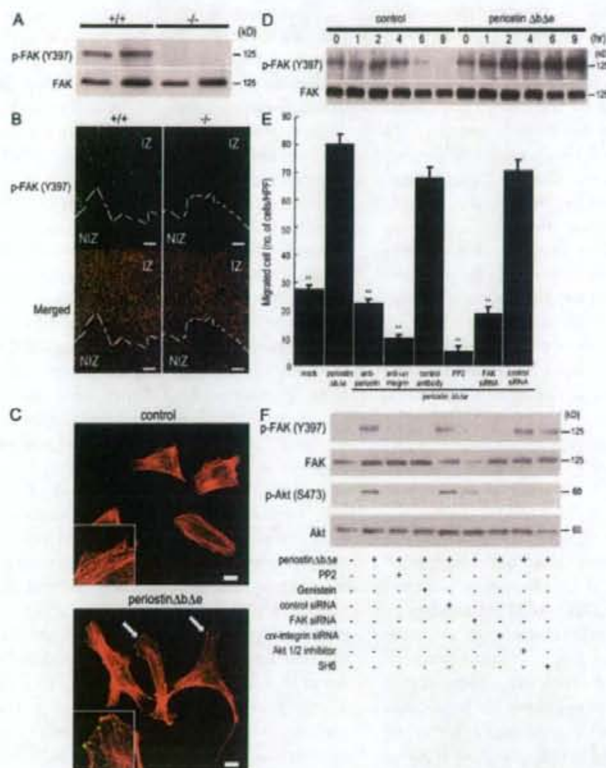

Figure 4. Periostin promotes cell migration through integrin-mediated FAK signaling. (A) Phosphorylation of FAK in infarct LV from *periostin*$^{+/+}$ mice and $^{-/-}$ mice 5 d after AMI. (B) Immunofluorescence for phosphorylated FAK (p-FAK^{Y397}) in the border of infarct LV from *periostin*$^{+/+}$ mice and $^{-/-}$ mice 5 d after AMI. Merged images show an overlay of p-FAK^{Y397} (green) and propidium iodide–stained nuclei (red). The dotted line shows the infarct border. NIZ, noninfarct zone; IZ, infarct zone. (C and D) Promotion of cell spreading and activation of FAK phosphorylation in vitro. The morphology of starved C3H10T1/2 cells was analyzed by immunofluorescence 12 h after adding periostin ΔbΔe (C), and the p-FAK^{Y397} was examined by Western blot analysis at various times after adding periostin ΔbΔe (D). In C, the merged images show an overlay of p-FAK^{Y397} (green) and rhodamine-phalloidin (red), and the arrows point to FAK phosphorylation sites. The insets show higher magnification of the cell processes. (E) Chemotaxis of primary cardiac fibroblasts from *periostin*$^{-/-}$ mice in the absence (mock) or presence of periostin ΔbΔe, detected by an in vitro cell migration assay. Cardiac fibroblasts were significantly activated by periostin ΔbΔe, and treatment with neutralizing antibodies against periostin and αv-integrin, PP2, or FAK siRNAs reduced the cell migration. **, $P < 0.001$ vs. periostin ΔbΔe. Error bars represent the mean ± the SEM. (F) Periostin can stimulate FAK and Akt phosphorylation through integrin signaling. Starved C3H10T1/2 cells were incubated for 1 h with periostin ΔbΔe with or without each siRNA or the FAK and Akt inhibitors. Bars: (B) 100 μm; (C) 20 μm.

Downloaded from jem.rupress.org on June 11, 2009

experiment, periostin ΔbΔe continuously activated the phosphorylation of FAK for 9 h after the addition of it to serum-starved cell cultures, whereas in the control, the signal had decreased by 6 h (Fig. 4 D). These results demonstrate that periostin ΔbΔe activated FAK phosphorylation and promoted formation of dynamic protrusions. Next, we tested the motility of primary cardiac fibroblasts from *periostin*$^{-/-}$ mice in the presence of periostin ΔbΔe. The result showed that periostin ΔbΔe strongly activated the cell migration of these fibroblasts (Fig. 4 E). Moreover, this migration caused by periostin ΔbΔe was significantly reduced by antibodies against either periostin or αv-integrin; by PP2, which is known as a compound that specifically inhibits adhesion-induced FAK phosphorylation (28); and by knockdown of FAK by siRNA (Fig. 4 E), suggesting that periostin ΔbΔe would activate the cell motility of their fibroblasts by FAK signaling through αv-integrin in mice subjected to AMI. Finally, we inhibited the integrin-mediated FAK pathway by using chemical compounds and siRNAs (Fig. 4 F). FAK inhibitors or siRNA down-regulated the Akt phosphorylation, and Akt inhibitors did not change FAK phosphorylation after stimulation by periostin ΔbΔe, indicating that Akt is a downstream molecule of FAK and periostin ΔbΔe. Moreover, αv-integrin siRNA treatment blocked both FAK and Akt phosphorylation after stimulation by periostin ΔbΔe. These results indicate that periostin ΔbΔe can stimulate FAK and Akt phosphorylation through αv-integrin.

We demonstrated that in the case of periostin deficiency, the collagen amount was reduced in the infarct myocardium, resulting in frequent cardiac rupture in the AMI. Our results, together with the previous findings by Norris et al. (7) on the role of periostin in collagen fibrillogenesis of skin and tendon, strongly suggest that fibrillar collagen formation, which contributes essentially to a mechanically stable scar formation, was impaired in the early stage of MI in the periostin deficiency, resulting in a high rate of cardiac rupture. Furthermore, we have found that the reduced mechanical strength, rupture of the infarct region, and repression of LV dilation in periostin deficiency were most likely caused by a reduced number of cardiac fibroblasts and by the insufficient creation of a durable collagen network caused by a lower rate of collagen synthesis and cross-linking. To reveal more about the importance of collagen production or collagen cross-linking for protection against heart rupture, after AMI, we treated mice with an inhibitor of lysyl oxidase, thus inhibiting collagen cross-linking. Interestingly, the data showed a high amount of collagen production with a larger number of vimentin-positive cells in the infarct region, resulting in effective blockage of heart rupture (unpublished data). These data suggest that periostin-stimulated migration of cardiac fibroblasts into the infarct region, the cells of which produce a high amount of collagen, is more essential than collagen cross-linking by periostin.

The expression of TGFβ was markedly up-regulated in the infarct border during the scar formation phase after AMI, and the phosphorylation of smad 2/3 was consequently increased (unpublished data), whereas there was no significant difference in the TGFβ transcription level between *periostin*$^{+/+}$ and $^{-/-}$ mice; TGFβ also enhanced the periostin expression in the infarct border after AMI because anti-TGFβ antibody treatment blocked the periostin expression (Fig. S6, available at http://www.jem.org/cgi/content/full/jem.20071297/DC1). The expression of both TGFβ and periostin is up-regulated by angiotensin II and attenuated by angiotensin receptor blockers after AMI (29, 30), suggesting that periostin may play a role via angiotensin II-TGFβ signaling. The combined results on the biomechanical properties and the collagen content of the isolated infarct heart support the concept that the periostin-linked collagen fibrous skeleton is an important determinant of cardiac rupture.

The results given here indicate that periostin signals activate cell migration of cardiac fibroblasts from outside into the infarct region through FAK phosphorylation, and then the migrated cells differentiate into αSMA-positive fibroblasts, resulting in strengthening of the stiffness of the LV wall through collagen synthesis after AMI. FAK is known to be involved in tyrosine phosphorylation during integrin-mediated signaling, and this molecule plays an important role in the response of migrating cells to mechanical stress (31). Recently, FAK has been implicated as a downstream target associated with angiotensin II–stimulated cell migration (32). The mechanism underlying the periostin action of promoting the recruitment of cardiac fibroblasts followed by healing of the infarct region appears to involve activation of the FAK pathway, indicating that the periostin-induced increase in FAK phosphorylation in the infarct myocardium enhanced the motility of these fibroblasts. In contrast, three-dimensional culture studies imply that the matrix stiffness regulates cell fate by modulating integrin signaling (31, 33). Considering these accumulated results, we suggest that periostin is mainly produced by fibroblasts through angiotensin II–TGFβ signaling and may convey pathologically rapid reinforced mechanical signals to FAK-integrin signaling after AMI. The fibroblastic cells activated by these signals secrete periostin, which in turn increases their motility, contractility, and synthesis of ECM proteins, thus promoting further recruitment and activation of fibroblasts. Periostin may serve as the trigger of these feedback mechanisms in the ongoing healing processes. Additional studies to elucidate in more detail the characteristics of cardiac fibroblasts may lead to a deeper understanding of the role of periostin after AMI, as well as aid in identifying the molecular targets of therapies to augment cardiac performance and wall stiffness after AMI.

MATERIALS AND METHODS

Preparation of rabbit polyclonal antibodies against periostin. We raised polyclonal RD1 antibodies against periostin by using the peptide DNLDSDIRRGLESNVN (representing aa 143–158 of human periostin) for human periostin and the peptide ENLDSDIRRGLENNVN (representing aa 145–160 of mouse periostin) for mouse periostin. The antibodies were affinity-purified by using the respective immunogenic peptide.

Histology, immunostaining, and electron microscopy. Human tissue samples were obtained during autopsy and fixed in 4% neutral formalin or 20% formalin. A total of 41 cases, ranging from a fetus to an 89-yr-old patient, including 15 cases of myocardial infarction, were examined. All the cases were approved for use in research by the Ethics Committee of the

Downloaded from jem.rupress.org on June 11, 2009

Published January 21, 2008

JEM

University of Tokyo. After having been embedded in paraffin, specimens were cut at a 4-μm thickness. Hematoxylin and eosin, elastica von Gieson, and Azan staining procedures were performed. Immunohistochemistry by the ABC method was done by using an i6000 apparatus (Biogenex).

For histological analysis of the infarcted mice, the animals were killed at 1, 2, 3, 4, 5, 7, 14, or 28 d after surgery under anesthesia, and were perfusion fixed with 4% paraformaldehyde at physiological pressure. Fixed hearts were sectioned transversely into three equal segments from their apex to base and cryoembedded or embedded in paraffin. 4-μm-thick sections were used for histological analysis or for immunostaining. Antibodies against αv-integrin (Laboratory Vision), αSMA (Sigma-Aldrich), FAK (BD Biosciences), pY397FAK (Invitrogen), pS473Akt (Cell Signaling Technology), Akt (Cell Signaling Technology), collagen I (Novotec), fibronectin (34), Ki67 (YLEM), active caspase3 (Promega), vimentin (PROGEN), smooth muscle myosin-1 (SM1; Kyowa Hakko Ltd.), and Mac3 (BD Biosciences) were used for immunostaining. Antigen unmasking techniques were not performed, except for anti–αv-integrin. For immunostaining of pY397FAK and pS473Akt, the Catalyzed Signal Amplification system was used (Dako). In the case of fluorescence studies, the signals were observed under a confocal microscope (FLUOVIEW FV1000; Olympus).

Sections of infarcted heart were generated from 6 *periostin*$^{+/+}$ and 6 $^{-/-}$ male mice at 5 and 28 d after AMI, and they were prepared for electron microscopy as previously described (35). Sham-operated mice were used for the control. Collagen fibril diameters were measured in scanned images generated from electron micrographs with Image J software. Collagen fibrils and the number of vimentin-positive or αSMA-positive cells in at least 6 fields derived from each of the basement-, mid-, and apex-part of the infarct region of heart sections were quantified (6 mice per group). Animal studies were conducted under a protocol approved by the Institutional Animal Use and Care Committee.

Quantification of collagen cross-links and collagen contents. Snap-frozen infarct tissues from *periostin*$^{+/+}$ and $^{-/-}$ mice were used. Pyridinoline and hydroxyproline contents were determined by the previously described HPLC method (36).

Adenovirus-mediated gene transfer. Construction of Ad-nlsLacZ and Ad-periostin ΔbΔe vectors was performed by use of an Adeno-X Expression System 2 (BD Biosciences). The virus purification method used, involving cesium chloride ultracentrifugation, was previously described (37). 1 d before LAD ligation, a volume of 100 μl containing 1.6×10^{10} PFU of Ad-nls-LacZ or Ad-periostin ΔbΔe virus was injected into a tail vein of male *periostin*$^{-/-}$ mice.

Statistical analysis. All numerical results were presented as the mean ± the SEM. Statistical analyses of the echocardiography and cell migration assay were performed with a Student's unpaired *t* test. Cardiac rupture frequency was compared by the χ^2 test. Survival curves after AMI were obtained by the Kaplan-Meier method, and compared by the log-rank test. Differences were considered significant at $P < 0.05$.

Online supplemental material. Fig. S1 shows the confirmation of the periostin expression in cardiac fibroblasts. Fig. S2 indicates the generation of *periostin*$^{-/-}$ mice. Fig. S3 shows the immunofluorescence analysis of fibronectin after AMI. Fig. S4 shows immunofluorescence analysis for gene-transferred *periostin*$^{-/-}$ infarct heart. Fig. S5 depicts the analysis for the phosphorylation of Akt after AMI. Fig. S6 shows a cause-and-effect relationship between TGFβ and periostin after AMI. Table S1 provides the echocardiographic data. Full methods and associated references are available in the Supplemental materials and methods. The online version of this article is available at http://www.jem.org/cgi/content/full/jem.20071297/DC1.

The authors thank M. Ikumi and E. Ikeno for technical assistance in generating knockout mice; S. Matsumura and M. Yoshioka for their technical help in the LV rupture threshold study; and S. Sakaguchi for her support, patience, and comprehension.

This research was supported by grants-in-aid from the Ministry of Education, Culture, Sports, Science, and Technology of Japan to A. Kudo and Y. Saga.

The authors have no conflicting financial interests.

Submitted: 25 June 2007
Accepted: 17 December 2007

REFERENCES

1. Horiuchi, K., N. Amizuka, S. Takeshita, H. Takamatsu, M. Katsuura, H. Ozawa, Y. Toyama, L.F. Bonewald, and A. Kudo. 1999. Identification and characterization of a novel protein, periostin, with restricted expression to periosteum and periodontal ligament and increased expression by transforming growth factor beta. *J. Bone Miner. Res.* 14:1239–1249.
2. Gillan, L., D. Matei, D.A. Fishman, C.S. Gerbin, B.Y. Karlan, and D.D. Chang. 2002. Periostin secreted by epithelial ovarian carcinoma is a ligand for alpha(V)beta(3) and alpha(V)beta(5) integrins and promotes cell motility. *Cancer Res.* 62:5358–5364.
3. Bao, S., G. Ouyang, X. Bai, Z. Huang, C. Ma, M. Liu, R. Shao, R.M. Anderson, J.N. Rich, and X.F. Wang. 2004. Periostin potently promotes metastatic growth of colon cancer by augmenting cell survival via the Akt/PKB pathway. *Cancer Cell.* 5:329–339.
4. Lindner, V., Q. Wang, B.A. Conley, R.E. Friesel, and C.P.H. Vary. 2005. Vascular injury induces expression of periostin: implications for vascular cell differentiation and migration. *Arterioscler. Thromb. Vasc. Biol.* 25:77–83.
5. Li, G., S. Oparil, J.M. Sanders, L. Zhang, M. Dai, L.B. Chen, S.J. Conway, C.A. McNamara, and I.J. Sarembock. 2006. Phosphatidylinositol-3-kinase signaling mediates vascular smooth muscle cell expression of periostin in vivo and in vitro. *Atherosclerosis.* 188:292–300.
6. Butcher, J.T., R.A. Norris, S. Hoffman, C.H. Mjaatvedt, and R.R. Markwald. 2007. Periostin promotes atrioventricular mesenchyme matrix invasion and remodeling mediated by integrin signaling through Rho/PI 3-kinase. *Dev. Biol.* 302:256–266.
7. Norris, R.A., B. Damon, V. Mironov, V. Kasyanov, A. Ramamurthi, R. Moreno-Rodriguez, T. Trusk, J.D. Potts, R.L. Goodwin, J. Davis, et al. 2007. Periostin regulates collagen fibrillogenesis and the biomechanical properties of connective tissues. *J. Cell. Biochem.* 101:695–711.
8. Kruzynska-Frejtag, A., M. Machnicki, R. Rogers, R.R. Markwald, and S.J. Conway. 2001. Periostin (an osteoblast-specific factor) is expressed within the embryonic mouse heart during valve formation. *Mech. Dev.* 103:183–188.
9. Stanton, L.W., L.J. Garrard, D. Damm, B.L. Garrick, A. Lam, A.M. Kapoun, Q. Zheng, A.A. Protter, G.F. Schreiner, and R.T. White. 2000. Altered patterns of gene expression in response to myocardial infarction. *Circ. Res.* 86:939–945.
10. Urasawa, K., I. Yoshida, C. Takagi, H. Onozuka, T. Mikami, H. Kawaguchi, and A. Kitabatake. 1996. Enhanced expression of beta-adrenergic receptor kinase 1 in the hearts of cardiomyopathic Syrian hamsters, BIO53.58. *Biochem. Biophys. Res. Commun.* 219:26–30.
11. Wang, D., S. Oparil, J.A. Feng, P. Li, G. Perry, L.B. Chen, M. Dai, S.W. John, and Y.F. Chen. 2003. Effects of pressure overload on extracellular matrix expression in the heart of the atrial natriuretic peptide-null mouse. *Hypertension.* 42:88–95.
12. Katsuragi, N., R. Morishita, N. Nakamura, T. Ochiai, Y. Taniyama, Y. Hasegawa, K. Kawashima, Y. Kaneda, T. Ogihara, and K. Sugimura. 2004. Periostin as a novel factor responsible for ventricular dilation. *Circulation.* 110:1806–1813.
13. Bujak, M., and N.G. Frangogiannis. 2007. The role of TGF-beta signaling in myocardial infarction and cardiac remodeling. *Cardiovasc. Res.* 74:184–195.
14. Sun, Y., and K.T. Weber. 2000. Infarct scar: a dynamic tissue. *Cardiovasc. Res.* 46:250–256.
15. Virag, J.I., and C.E. Murry. 2003. Myofibroblast and endothelial cell proliferation during murine myocardial infarct repair. *Am. J. Pathol.* 163:2433–2440.
16. Tomasek, J.J., G. Gabbiani, B. Hinz, C. Chaponnier, and R.A. Brown. 2002. Myofibroblasts and mechano-regulation of connective tissue remodelling. *Nat. Rev. Mol. Cell Biol.* 3:349–363.
17. Heymans, S., A. Luttun, D. Nuyens, G. Theilmeier, E. Creemers, L. Moons, G.D. Dyspersin, J.P.M. Cleutjens, M. Shipley, A. Angellilo,

Downloaded from jem.rupress.org on June 11, 2009

et al. 1999. Inhibition of plasminogen activators or matrix metalloproteinases prevents cardiac rupture but impairs therapeutic angiogenesis and causes cardiac failure. *Nat. Med.* 5:1135–1142.

18. Matsumura, S.-I., S. Iwanaga, S. Mochizuki, H. Okamoto, S. Ogawa, and Y. Okada. 2005. Targeted deletion or pharmacological inhibition of MMP-2 prevents cardiac rupture after myocardial infarction in mice. *J. Clin. Invest.* 115:599–609.
19. Matsusaka, H., T. Ide, S. Matsushima, M. Ikeuchi, T. Kubota, K. Sunagawa, S. Kinugawa, and H. Tsutsui. 2006. Targeted deletion of p53 prevents cardiac rupture after myocardial infarction in mice. *Cardiovasc. Res.* 70:457–465.
20. Nahrendorf, M., K. Hu, S. Frantz, F.A. Jaffer, C.-H. Tung, K.-H. Hiller, S. Voll, P. Nordbeck, D. Sosnovik, S. Gattenlohner, et al. 2006. Factor XIII deficiency causes cardiac rupture, impairs wound healing, and aggravates cardiac remodeling in mice with myocardial infarction. *Circulation.* 113:1196–1202.
21. Askari, A.T., M.-L. Brennan, X. Zhou, J. Drinko, A. Morehead, J.D. Thomas, E.J. Topol, S.L. Hazen, and M.S. Penn. 2003. Myeloperoxidase and plasminogen activator inhibitor 1 play a central role in ventricular remodeling after myocardial infarction. *J. Exp. Med.* 197:615–624.
22. Sun, M., F. Dawood, W.-H. Wen, M. Chen, I. Dixon, L.A. Kirshenbaum, and P.P. Liu. 2004. Excessive tumor necrosis factor activation after infarction contributes to susceptibility of myocardial rupture and left ventricular dysfunction. *Circulation.* 110:3221–3228.
23. Ichihara, S., T. Senbonmatsu, E. Price Jr., T. Ichiki, F.A. Gaffney, and T. Inagami. 2002. Targeted deletion of angiotensin II type 2 receptor caused cardiac rupture after acute myocardial infarction. *Circulation.* 106:2244–2249.
24. Michael, L.H., M.L. Entman, C.J. Hartley, K.A. Youker, J. Zhu, S.R. Hall, H.K. Hawkins, K. Berens, and C.M. Ballantyne. 1995. Myocardial ischemia and reperfusion: a murine model. *Am. J. Physiol.* 269:H2147–H2154.
25. Lindsley, A., W. Li, J. Wang, N. Maeda, R. Rogers, and S.J. Conway. 2005. Comparison of the four mouse fasciclin-containing genes expression patterns during valvuloseptal morphogenesis. *Gene Expr. Patterns.* 5:593–600.
26. Stambolic, V., and J.R. Woodgett. 2006. Functional distinctions of protein kinase B/Akt isoforms defined by their influence on cell migration. *Trends Cell Biol.* 16:461–466.
27. Mitra, S.K., D.A. Hanson, and D.D. Schlaepfer. 2005. Focal adhesion kinase: in command and control of cell motility. *Nat. Rev. Mol. Cell Biol.* 6:56–68.
28. Hakuno, D., T. Takahashi, J. Lammerding, and R.T. Lee. 2005. Focal adhesion kinase signaling regulates cardiogenesis of embryonic stem cells. *J. Biol. Chem.* 280:39534–39544.
29. Iekushi, K., Y. Taniyama, J. Azuma, N. Katsuragi, N. Dosaka, F. Sanada, N. Koibuchi, K. Nagao, T. Ogihara, and R. Morishita. 2007. Novel mechanisms of valsartan on the treatment of acute myocardial infarction through inhibition of the antiadhesion molecule periostin. *Hypertension.* 49:1409–1414.
30. Berk, B.C., K. Fujiwara, and S. Lehoux. 2007. ECM remodeling in hypertensive heart disease. *J. Clin. Invest.* 117:568–575.
31. Wang, H.-B., M. Dembo, S.K. Hanks, and Y.-l. Wang. 2001. Focal adhesion kinase is involved in mechanosensing during fibroblast migration. *Proc. Natl. Acad. Sci. USA.* 98:11295–11300.
32. Baudino, T.A., W. Carver, W. Giles, and T.K. Borg. 2006. Cardiac fibroblasts: friend or foe? *Am. J. Physiol. Heart Circ. Physiol.* 291:H1015–H1026.
33. Bershadsky, A.D., N.Q. Balaban, and B. Geiger. 2003. Adhesion-dependent cell mechanosensitivity. *Annu. Rev. Cell Dev. Biol.* 19:677–695.
34. Arai, S., N. Amizuka, Y. Azuma, S. Takeshita, and A. Kudo. 2003. Osteoclastogenesis-related antigen, a novel molecule on mouse stromal cells, regulates osteoclastogenesis. *J. Bone Miner. Res.* 18:686–695.
35. Kii, I., N. Amizuka, L. Minqi, S. Kitajima, Y. Saga, and A. Kudo. 2006. Periostin is an extracellular matrix protein required for eruption of incisors in mice. *Biochem. Biophys. Res. Commun.* 342:766–772.
36. Saito, M., K. Marumo, K. Fujii, and N. Ishioka. 1997. Single-column high-performance liquid chromatographic-fluorescence detection of immature, mature, and senescent cross-links of collagen. *Anal. Biochem.* 253:26–32.
37. Ugai, H., T. Yamasaki, M. Hirose, K. Inabe, Y. Kujime, M. Terashima, B. Liu, H. Tang, M. Zhao, T. Murata, et al. 2005. Purification of infectious adenovirus in two hours by ultracentrifugation and tangential flow filtration. *Biochem. Biophys. Res. Commun.* 331:1053–1060.

Downloaded from jem.rupress.org on June 11, 2009

nature cell biology

MesP1 drives vertebrate cardiovascular differentiation through Dkk-1-mediated blockade of Wnt-signalling

R. David[1], C. Brenner[1,7], J. Stieber[2], F. Schwarz[1], S. Brunner[1], M. Vollmer[3], E. Mentele[4], J. Müller-Höcker[5], S. Kitajima[6], H. Lickert[3], R. Rupp[4] and W.-M. Franz[1]

ES-cell-based cardiovascular repair requires an in-depth understanding of the molecular mechanisms underlying the differentiation of cardiovascular ES cells. A candidate cardiovascular-fate inducer is the bHLH transcription factor MesP1[1,2]. As one of the earliest markers, it is expressed specifically in almost all cardiovascular precursors and is required for cardiac morphogenesis[2,3]. Here we show that MesP1 is a key factor sufficient to induce the formation of ectopic heart tissue in vertebrates and increase cardiovasculogenesis by ES cells. Electrophysiological analysis showed all subtypes of cardiac ES-cell differentiation[4]. MesP1 overexpression and knockdown experiments revealed a prominent function of MesP1 in a gene regulatory cascade, causing Dkk-1-mediated blockade of canonical Wnt-signalling. Independent evidence from ChIP and *in vitro* DNA-binding studies, expression analysis in wild-type and *MesP* knockout mice, and reporter assays confirm that *Dkk-1* is a direct target of MesP1. Further analysis of the regulatory networks involving MesP1 will be required to preprogramme ES cells towards a cardiovascular fate for cell therapy and cardiovascular tissue engineering. This may also provide a tool to elicit cardiac transdifferentiation in native human adult stem cells.

Current therapeutic modalities for degenerative cardiovascular diseases are limited. They include medical therapy, mechanical left-ventricular assist devices and cardiac transplantation. Embryonic stem (ES) cells, which can differentiate into functional cardiovascular cells, may enable transplantation of cardiovascular cells [5]. The proliferative potential of cardiomyocytes derived from ES cells is limited, and reasonable yields to repair an infarction in humans (>10^9 cardiomyocytes) are yet to be achieved[6].

It is crucial, therefore, to understand the biological processes leading to formation of cardiovascular cells. A candidate key cardiovascular-fate inducer is the basic helix-loop-helix (bHLH) transcription factor, MesP1, which is expressed in almost all precursors of the cardiovascular system. It is required for cardiac morphogenesis and is currently the earliest marker of the cardiovascular lineage[1,2,7]. MesP1-deficient mice show aberrant heart morphogenesis that resulted in cardia bifida[1] and misexpression of Flk1 (VEGFR-2 or KDR), one of the receptors for VEGF[1]. In the primitive chordate *Ciona savignyi*, the sole known orthologue of vertebrate *MesP* genes in ascidians (*Cs-MesP*) is essential for specification of heart precursor cells expressing *Nkx*, *HAND* and *HAND*-like genes. Morpholino-based knockdown of *Cs-MesP* causes failure of the development of the juvenile heart[8]. A constitutively active Cs-MesP induced cardiogenesis independently of cardiac precursor-cell migration in *Ciona*[8]. This suggests a mechanism for cardiovascular specification that is highly conserved in chordates and initiated by *MesP* genes, with factors such as Nkx, HAND and Flk1 acting further downstream.

We therefore hypothesized that cardiovasculogenesis in vertebrates not only requires correct MesP1 expression, but also that this factor might be a master regulator sufficient to induce cardiovasculogenesis. Here, we show from different experimental systems using vertebrate embryos, as well as ES cells and *in vitro* studies, that this is indeed the case.

We first injected MesP1 overexpression-plasmid DNA into one blastomere of two-cell *Xenopus laevis* embryos. This caused the formation of ectopic beating tissue in various regions of developed tadpoles (Supplementary Information, Movies 1–4). The beating rhythm of the specimen (Supplementary Information, Movie 1) indicated that the contracting tissue in the head region was electrically coupled to the heart, whereas ectopic beating (Supplementary Information, movies Movies 2, 3) showed autonomous rhythms. Whole-mount *in situ* hybridization for myosin light chain (MLC) mRNA confirmed ectopic formation of cardiomyocytes in tadpoles that overexpressed MesP1 (Fig. 1b–e), compared with control tadpoles (Fig. 1a).

Relying on the high conservation of vertebrate MesP1 proteins, we used human MesP1 in mouse ES cells as it would be easily traced. We inserted human *MesP1* cDNA in pIRES–EGFP-2 for overexpression in ES cells (Fig. 2a), simultaneously allowing detection of ES-cell clones using

[1]Medizinische Klinik und Poliklinik I, Klinikum Großhadern der LMU, D-81377 München, Germany. [2]Lehrstuhl für Pharmakologie und Toxikologie der Universität Erlangen, D-91054 Erlangen, Germany; [3]GSF - National Research Center for Environment and Health, D-85764 Neuherberg, Germany. [4]Adolph-Butenandt-Institut der LMU, D-80336 München, Germany. [5]Pathologisches Institut der LMU, D-80337 München, Germany. [6]Division of Cellular & Molecular Toxicology, Biological Safety Research Center, National Institute of Health Sciences 1-18-1 Kamiyohga, Setagaya-ku, Tokyo 158-8501, Japan.
Correspondence should be addressed to R.D. or W.-M.F. (e-mail: robert.david@med.uni-muenchen.de; wolfgang.franz@med.uni-muenchen.de)

Received 6 December 2007; accepted 28 January 2008; published online 24 February 2008; DOI: 10.1038/ncb1696

© 2008 Nature Publishing Group

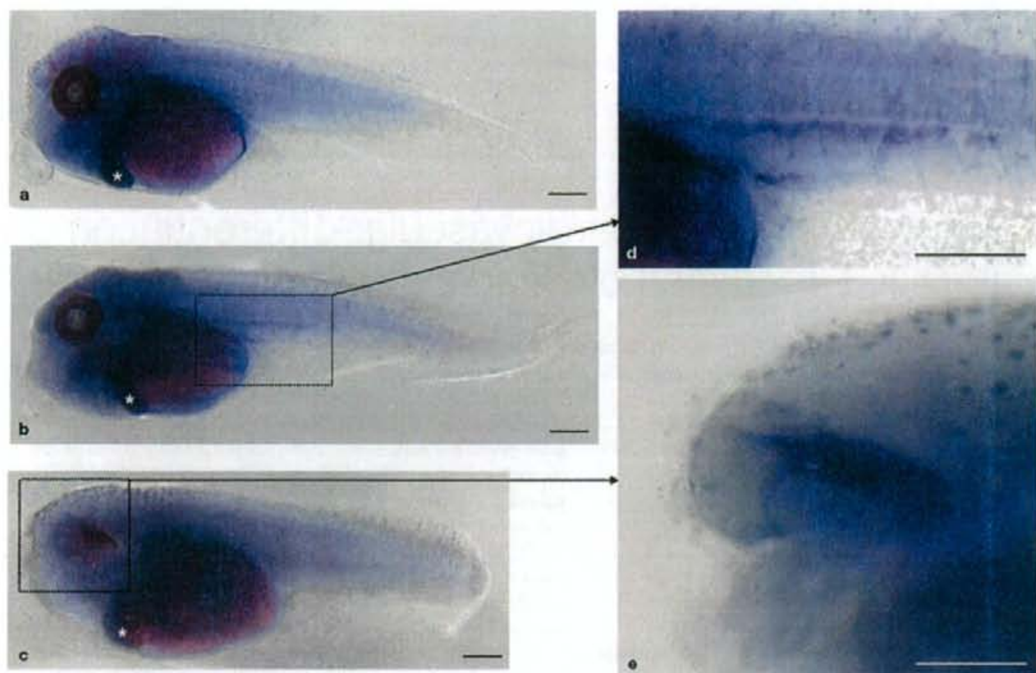

Figure 1 MesP1 overexpression in *Xenopus* induces ectopic cardiac tissue. **(a)** MLC *in situ* hybridization using a stage 45 *Xenopus* control tadpole previously injected with 100 pg EGFP expression plasmid into one blastomere at two-cell stage. * Specific staining of *MLC* mRNA within the heart. **(b, c)** MLC *in situ* hybridization using stage 45 *Xenopus* tadpoles injected with 100 pg MesP1 overexpression plasmid. Specific staining of *MLC* mRNA in the heart (*) was paralleled by MLC expression in the trunk region (b, boxed area) and in the dorsal part of a partially ablated eye on the injected side (c, boxed area). **(d)** Higher magnification of ectopic MLC expression in specimen b. **(e)** Higher magnification of MLC expression in the eye region shown for specimen c. Scale bars are 0.5 mm.

EGFP (enhanced green fluorescent protein; Fig. 2b, c). Overexpression of MesP1 was confirmed at the mRNA (Fig. 2d) and protein levels (Fig. 2e). RT-PCRs showed no influence on *Oct4*, *Nanog* and *Rex-1* mRNA levels, compared with control transfected cells, which were normal, undifferentiated colonies grown in medium containing leukaemia inhibitory factor (LIF; Fig. 2f). These results suggest that MesP1 alone is not sufficient to induce germ-layer-specific differentiation.

We then verified the time course of cytomegalovirus (CMV) promoter activity used in our overexpression construct: fluorescence activated cell sorting (FACS) analyses for EGFP expression showed that 89% of the cells were EGFP-positive at day 0 of differentiation and 12% were positive at day 4 (Supplementary Information, Fig. S1). This is consistent with the known silencing of the CMV promoter in differentiating ES cells.

During differentiation, clones that overexpressed MesP1 began to contract earlier and showed approximately five-fold more contracting areas, compared with the controls (Fig. 3a, Supplementary Information, Movies 5, 6). This exceeds the *in vitro* yield reported in previous studies, in which, ES-cell-derived cardiomyocytes were increased two- to three-fold by treatment with retinoic acid[10], nitric oxide or an inducible nictic oxide synthase[11]. Similarly, in a study where cells had to be preselected for Flk1 using FACS[12], increased cardiomyogenesis was observed in ES cells lacking RBP-J, a key downstream element in the Notch signalling pathway.

Cardiomyocytes that overexpressed MesP1 showed normal patterns of the cardiac sarcomeric marker αMHC (Fig. 3b–d). Ultrastructure of the cells with typical myocytic features revealed parallel arrays of myofibrillar bundles inserting into Z-disc-like bands (Fig. 3e). Similarly, intercellular contacts, probably corresponding to gap junctions, were detected (Fig. 3f).

In addition to increased beating, the MesP1-transfected ES-cell clones showed highly increased spontaneous sprouting of structures from embryoid bodies (EBs), which resembled vascular cells (Fig. 3g–j), a feature normally induced in sprouting assays by addition of VEGF, FGF2 and erythropoietin in collagen I gel matrices[13]. These cells migrated out of the EBs and showed typical expression of von Willebrand factor (vWF; Fig. 3h, i). Our observation is consistent with the knowledge that cardiac and vascular cells share the same embryonic origin in the lateral plate mesoderm and that mouse MesP1 has been described as a marker for both cardiac- and endothelial-cell precursors[1].

We next investigated whether our observations are consistent with mRNA expression patterns and found enhanced expression of transcripts encoding the early cardiac transcription factors Nkx 2.5, GATA 4 and Mef2c (Fig. 4a). mRNAs encoding the cardiac structural proteins and hormones connexin 45, connexin 43, MLC2v, TnI, ANF and TTR, were markedly increased (Fig. 4a). Additionally, at day 6, mRNA levels

© 2008 Nature Publishing Group

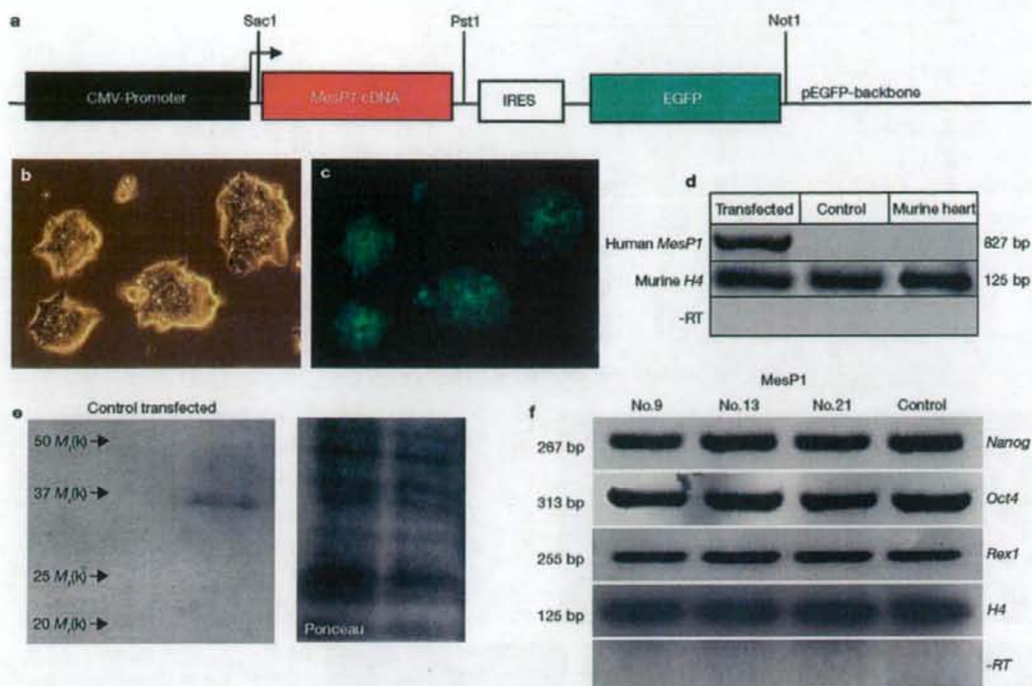

Figure 2 Functionality of the MesP1 overexpression construct in ES cells. (**a**) Transfection construct bearing the human *MesP1-IRES-EGFP* cassette. (**b**, **c**) Stably transfected mouse ES cell colonies showing EGFP fluorescence. (**d**) RT-PCR for overexpressed human *MesP1* mRNA in stably transfected mouse ES cells. (**e**) Verification of hMesP1 overexpression in mouse ES cells on the protein level. Full scans shown in Supplementary Information, Fig. S6. (**f**) RT-PCR using cDNA from undifferentiated ES cell clones: relative expression levels of pluripotency markers in the presence of LIF show no difference compared with EGFP control transfected cells. Full scans shown in Supplementary Information, Fig. S6.

for VE-cadherin were increased (Fig. 4a), correlating with the increased vascular sprouting described above (Fig. 3g–j). Downregulation of the skeletal muscle marker MyoD was also observed, indicating a shift towards the lateral plate mesoderm (Fig. 4a). An increase in the number of cells expressing the proteins α-actinin, cardiac MLC-1, TnI and CD31 (PECAM) confirmed our mRNA data (Fig 4b–d; Supplementary Information, Fig. S4C).

In the non-mesodermal lineages, neural differentiation seemed to be increased in MesP1-overexpressing cells, as shown for *NeuroD* and *Neurogenin* mRNAs. Correspondingly, epidermis formation in ectodermal ES-cell descendents seemed to be diminished, as indicated by the decreased expression of cytokeratin17 (Fig. 4a). This observation is consistent with the known neural-inducing potential of cardiogenic cells[14]. Expression of hepatocyte nuclear factor 4 (HNF4) was not altered, suggesting that endodermal differentiation was unaffected (Fig. 4a).

Electrophysiological analysis of isolated beating cardiomyocytes revealed that the three main cell types described for the near-terminally differentiated state of EB cardiomyocyte development (namely, ventricle-like, atrial-like and sinoatrial/atrioventricular (pacemaker-like) cells, as well as intermediate cells) are present in preparations from MesP1-overexpressing ES-cell clones (Supplementary Information, Fig. S2, Table S1). The action potentials generated by the respective cell types of MesP1 and control cells did not differ significantly with respect to their distinct parameters, such as maximum diastolic potential, diastolic depolarization rate, upstroke velocity or action potential plateau duration, or in their reaction to β-adrenoceptor (isoprenaline) and muscarinic-receptor (carbachol) stimulation. This supports the notion of correct cardiomyocyte development. In knockdown experiments using human *MesP1*-specific short hairpin (sh) RNA, the appearance of beating foci in shRNA-expressing ('rescued') ES cells, was reversed to control levels (Supplementary Information, Fig. S4A, B), corresponding to a reduction of TnI-expressing cells to a level similar to control numbers (Supplementary Information, Fig. S4C).

To identify direct targets of MesP1, we next performed a ChIP screen with subsequent cloning and sequencing of the unknown precipitated DNA fragments[15]. We identified two regions derived from the mouse Dkk-1 upstream region containing classical bHLH-binding motifs, which are highly conserved in humans, chickens and zebrafish *Dkk-1* genes (Supplementary Information, Fig. S5A). We then verified their specific enrichment in the precipitated DNA using PCR (Fig. 5a) and performed electrophoretic mobility shift assays (EMSAs) to confirm specific MesP1-binding to these elements *in vitro* (Fig. 5b). To investigate the relevance of these observations *in vivo*, we performed whole-mount *in situ* hybridization using embryonic day (E) 7.5 mouse

© 2008 Nature Publishing Group

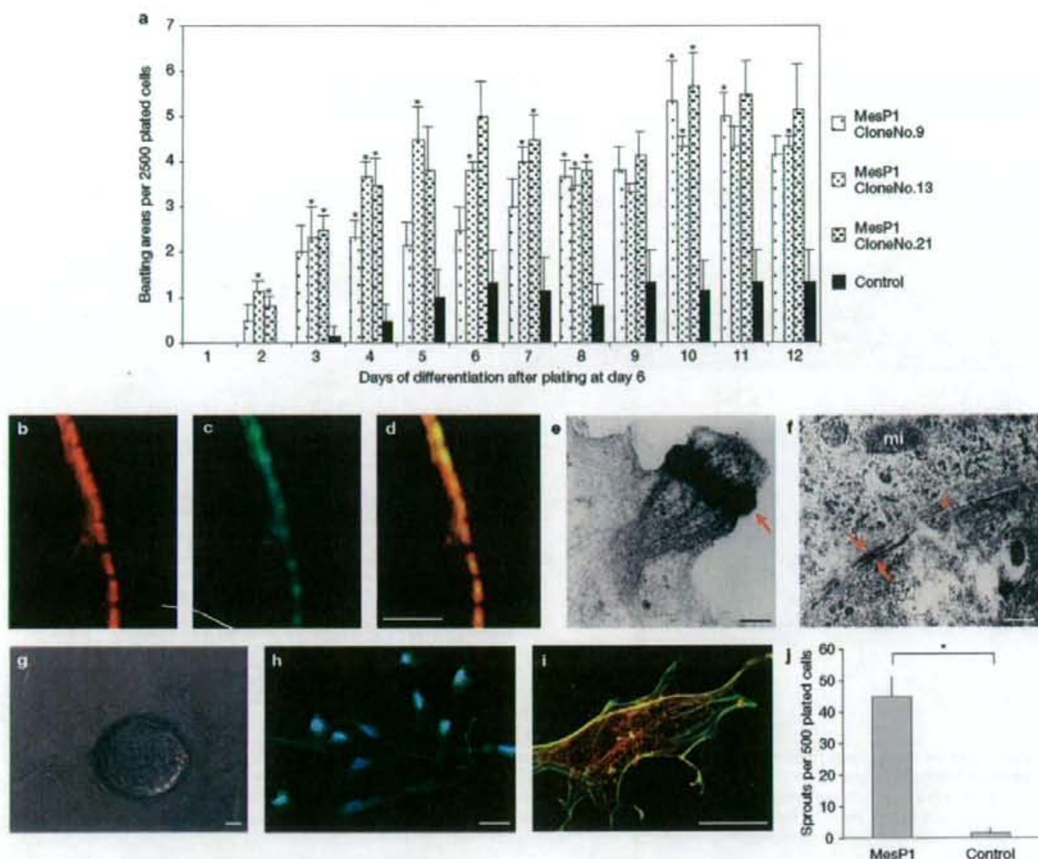

Figure 3 Increased appearance of cardiomyocytes and endothelial cells in MesP1-overexpressing ES cells. (**a**) Increase of spontaneous beating activity in three independent mouse ES cell clones stably transfected with the *MesP1–IRES–EGFP* construct. (**b**) Confocal analysis of αMHC expression in a cardiomyocyte overexpressing MesP1. (**c**) Counterstaining against actin. (**d**) Overlay of αMHC and actin staining. Scale bar is 5 μm. (**e**) Electron microscopy: straight fibrils composed predominantly of thick filaments (myosin) and formation of a Z-line (→) in the subplasmalemmal zone. Scale bar is 0.5 μm. (**f**) Intercellular junctions between two cells with subplasmalemmal densities (→) and longitudinal aggregates of thin filaments (*). The gap was narrowed at the contact sites, consistent with an attenuated gap junction. mi = Mitochondrium. Scale bar is 0.5 μm. (**g**) Spontaneous sprouting of vascular-like cells from an EB at day 10 of differentiation without any addition of angiogenic growth factors. Scale bar is 30 μm. (**h**) Staining of spontaneously sprouting vascular-like cells for vWF. Nuclei were counterstained with DAPI. Scale bar is 30 μm. (**i**) Overlay of confocal microscopic analysis of vWF expression (red) and actin expression (green) in spontaneously sprouting vascular like cells. Scale bar is 10 μm. (**j**) Quantification of spontaneous sprouting at day 10 of differentiation in MesP1-overexpressing and EGFP-overexpressing ES-cell clones (data are mean ± s. d., $n = 3$, $P = 0{,}0029$).

embryos, in which we found co-expression of MesP1 and Dkk-1 in the cardio-cranial mesoderm precursors[1] migrating laterally from the primitive streak towards the anterior region (Fig. 5c). Additionally, *MesP1* mRNA was found at the base of the allantois. At the same developmental stage, Dkk-1 was expressed in the anterior visceral endoderm, the anterior cardio-cranial mesoderm and at the base of the allantois (Fig. 5c, upper panels). Histological sections from these specimens show *MesP1* mRNA in posterior and lateral mesoderm populations giving rise to cardio-cranial mesoderm. Similarly, Dkk-1 was expressed in lateral and anterior cardio-cranial mesoderm populations (Fig. 5c, lower panels), demonstrating an overlapping expression domain with MesP-1 in this region.

We then analysed mRNA expression patterns at an earlier stage of ES-cell differentiation (day 3). Again, we found upregulation of *Nkx2.5* and *GATA4* mRNAs in ES cells overexpressing MesP1. In contrast to unaltered *brachyury* mRNA levels at day 3, the amounts of *Dkk-1* and *Hex* mRNAs were markedly increased (Fig. 5d).

To determine whether MesP1 can initiate cardiomyogenesis even in the absence of general mesoderm-inducing factors, we performed FACS analyses for Flk1, the earliest surface marker for the lateral mesoderm[16], during ES-cell differentiation. Few (0.2–0.25%) cells were found to express Flk1 in undifferentiated MesP1 and control clones. The Flk1-positive population did not increase significantly until day 4 of differentiation, when lateral and paraxial mesoderm have formed[17]. However,

© 2008 Nature Publishing Group

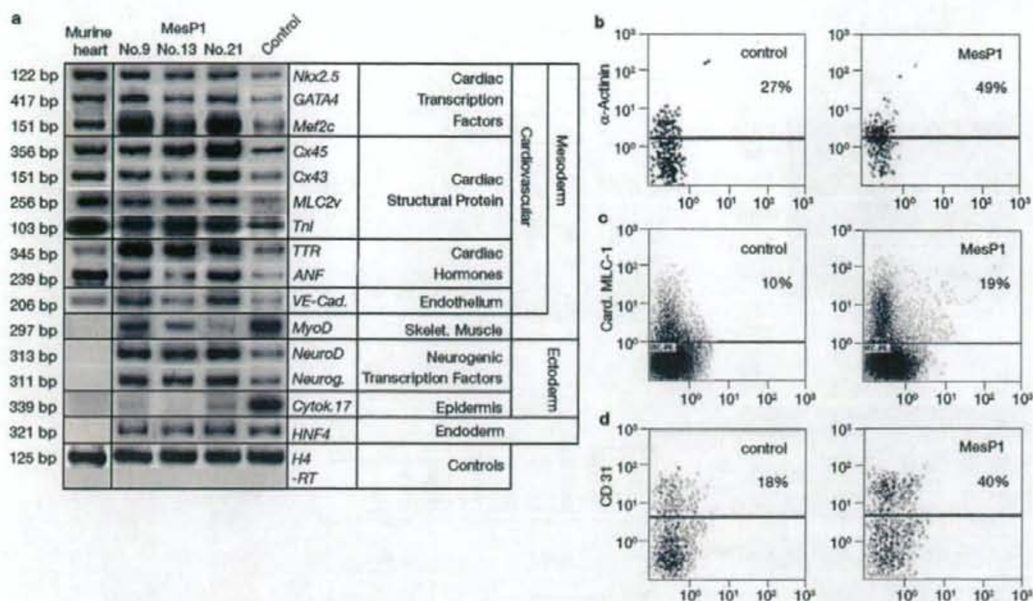

Figure 4 Increased expression of cardiovascular markers in MesP1-overexpressing ES cells. RT-PCR for mesodermal markers at day 6 of differentiation shows an increase in mRNA expression for cardiac markers Nkx 2.5, GATA 4, Mef2c, connexin 45, connexin 43, MLC2v, TnI, TTR and ANF in three independent *MesP1–IRES–EGFP* clones. In the same clones, mRNA for the endothelial marker VE-Cadherin was increased, whereas the skeletal muscle differentiation marker MyoD was decreased. In the ectodermal lineage *NeuroD* and *Neurogenin* mRNAs were increased, associated with decreased Cytokeratin17 expression. The endodermal marker HNF4 seemed to be unaffected. Full scans of key markers are shown in Supplementary Information, Fig. S6. (b) FACS analysis for α-actinin at day 18 of differentiation. Cells expressing α-actinin were increased 1.8-fold in MesP1 clones, compared with control transfected cells. (c) FACS analysis for cardiac MLC-1 at day 18 of differentiation. Cells expressing cardiac MLC-1 were increased 1.9-fold in MesP1 clones, compared with control transfected cells. (d) FACS analysis for CD31 (PECAM) at day 6 of differentiation. Cells expressing CD31 were increased 2-fold in MesP1 clones, compared with control transfected cells.

after this time-point, the increased cardiovascular differentiation in MesP1-overexpressing clones was confirmed by increases (approximately three-fold) in the Flk1-positive populations (Supplementary Information, Fig. S3). These data suggest that MesP1-based cardiogenesis depends on initial general mesoderm formation[18].

The results in Fig. 5d confirm that the cardiogenic effect of MesP1 is mediated by upregulation of the Wnt inhibitor Dkk-1. To verify our observations, reverse experiments were performed using stably expressed shRNA to knockdown endogenous MesP1. In two independent clones showing reduced MesP1 expression, this approach was accompanied by downregulation of *Dkk-1*, *Nkx2.5* and *GATA-4* mRNA expression (Fig. 5e). To extend the loss of function approach from ES cells to an *in vivo* setting, we performed whole-mount *in situ* hybridization with late gastrulae using wild-type and $MesP1^{-/-}$;$MesP2^{-/-}$ double knockout embryos[19]. In these embryos the absence of MesP expression led to loss of *Dkk-1* mRNA, specifically in the cardio-cranial mesoderm, caused by either silencing of Dkk-1 transcription or loss of these cells (Fig. 5f). Therefore, Dkk-1 expression in the anterior cardio-cranial mesoderm indeed is dependent on MesP function, whereas Dkk-1 expression in the anterior visceral endoderm and at the base of the allantois is MesP-independent.

To determine whether MesP1 is indeed a transcriptional activator, we performed luciferase assays using our mouse ES-cell lines. Each of the two MesP1 binding-site motifs derived from the *hDkk-1* promoter produced a six- to eight-fold increase in luciferase activity in MesP1-overexpressing cells (Fig. 5g). These results demonstrate that MesP1 acts as a transcriptional activator at the sites identified by ChIP-analysis. These findings were confirmed by *in vivo* experiments, where *hMesP1* mRNA or *hMesP1* expression plasmids were injected into the animal pole of two-cell *Xenopus* embryos, which were then subjected to quantitative RT-PCR analysis for *Dkk-1* mRNA at Nieuwkoop-Faber Stage 14 (Supplementary Information, Fig. S5B). Similarly, injections targeting the mesendoderm of four-cell *Xenopus* embryos showed increased *Dkk-1* mRNA levels (data not shown).

Recently, it has been shown that in *Xenopus*, Wnt antagonists stimulate cardiogenesis non-cell-autonomously, up to several cells away from those in which canonical Wnt/β-catenin signalling is blocked, indicative of an indirect role in heart induction. Dkk-1, which is found in defined mesodermal lineages, including the heart, and other inhibitors of the canonical Wnt pathway, induce Hex expression in endoderm underlying the presumptive cardiac mesoderm. Loss of Hex blocks endogenous cardiogenesis and ectopic heart induction by Dkk-1, whereas ectopic Hex induces expression of cardiac markers non-cell-autonomously[20]. Thus, to initiate cardiogenesis, Wnt antagonists act on endoderm to upregulate Hex, which, in turn, has been suggested to control the production of endoderm-derived, diffusible heart-inducing factors[18,20]. Our observation of a marked increase of *Hex* mRNA in MesP1-overexpressing ES

© 2008 Nature Publishing Group

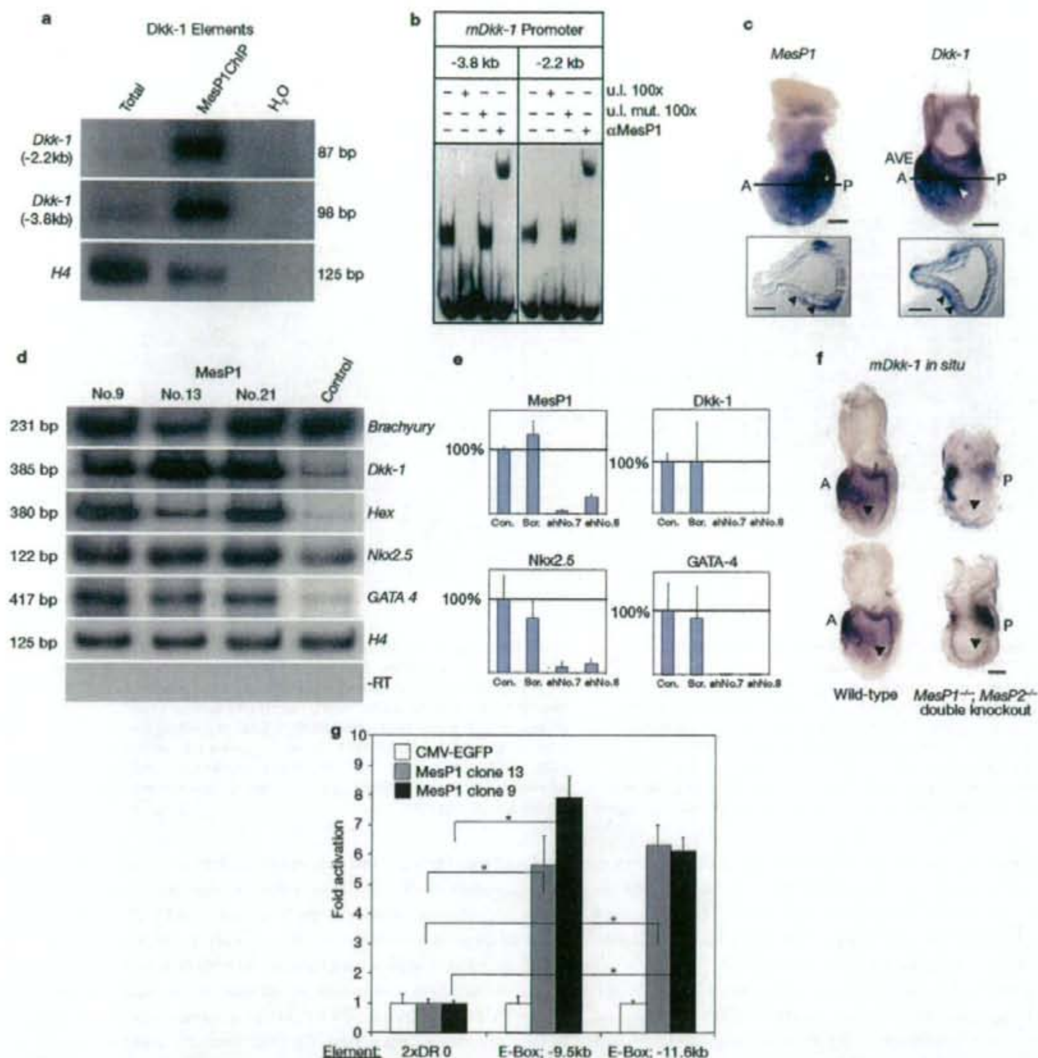

Figure 5 MesP1 enhances cardiovascular differentiation via Dkk-1 mediated blockage of Wnt-signalling. (**a**) PCRs from immunoprecipitated and total input DNA. Two *Dkk-1* promoter-derived PCR-fragments containing bHLH responsive elements were enriched. (**b**) EMSAs using nuclear ES cell extract and the isolated bHLH responsive elements. Lanes 1, 5: specific shift; lanes 2, 6: competition with 100× excess of unlabelled specific probe; lanes 3, 7: competition with 100× excess of unlabelled non-specific probe; lanes 4, 8: supershift. (**c**) Whole-mount samples from *in situ* hybridization of late gastrulae and cross-sections at the indicated level: *MesP1* and *Dkk-1* mRNAs were co-expressed in cardio-cranial mesoderm precursors. Left upper panel: MesP1 expression at E7.5 in mesoderm precursors migrating laterally from the primitive streak to give rise to cardio-cranial mesoderm. MesP1 was also expressed at the base of the allantois (*). Right upper panel: Dkk-1 expression in the anterior visceral endoderm (AVE), the anterior cardio-cranial mesoderm (arrowhead) and the base of the allantois. Sections show *MesP1*-mRNA (left lower panel) in posterior and lateral mesoderm, giving rise to cardio-cranial mesoderm. Right lower panel: Dkk-1 expression in lateral and anterior cardio-cranial mesoderm. Arrowheads: overlapping domains of MesP1 and Dkk-1. Scale bars are 150 μm. (**d**) RT-PCR from MesP1-ES cells (day 3 of differentiation): an increase of mRNA expression for GATA4 and Nkx2.5 but not brachyury was observed in three independent clones. Similarly, mRNAs for the Wnt inhibitor Dkk-1 and Hex were enhanced. Full scans shown in Supplementary Information, Fig. S6. (**e**) Knockdown of endogenous *MesP1* in ES cells using stably expressed shRNA caused reductions in *Dkk-1*, *Nkx2.5* and *GATA-4* mRNA levels (data are mean ± s. d., $n = 4$). (**f**) *In situ* hybridization of late gastrulae for Dkk-1 using wild-type (left) and $MesP1^{-/-}$;$MesP2^{-/-}$ double knockouts (right): in the knockouts, *Dkk-1* mRNA was specifically lost in the cardio-cranial mesoderm (arrowheads). Scale bar is 150 μm. (**g**) Luciferase assays using control and MesP1-overexpressing ES-cells. Each of the two conserved MesP1-binding sites (E-Box-9.5 kb; E-Box-11.6 kb) was sufficient to enhance luciferase expression 6–8 fold in hMesP1-overexpressing cells versus control ES cells. A control reporter gene containing a bHLH-half-site motif (2× DR 0) was not activated by MesP1 (data are mean ± s. d., $n = 5$, $^{*}P < 0.0025$).

© 2008 Nature Publishing Group

cells at day 3 of differentiation, leading to high levels of the cardiogenic markers Nkx2.5 and GATA-4, supports these findings (Fig. 5d). On the other hand, it was recently demonstrated that during the period of MesP1 expression, cardiogenic cells themselves are susceptible to Wnt-signalling, confirming that a precise amount and/or timing of Wnt/β-catenin signalling is required for formation of a proper heart tube[21].

In contrast to the requirement for inhibition of canonical Wnt-signalling at the onset of cardiogenesis, canonical Wnt-signalling seems to be required for the expansion and maturation of primary and secondary heart-field-derived cardiomyocytes during further development of the vertebrate heart[22,23]. This is reflected *in vivo* by Wnt8a expression from day 8.5 *post conceptionem* in mouse myocardium of the common ventricular and atrial chambers[24]. Our observation of a decrease in *Dkk-1* mRNA below detection levels in control as well as MesP1-overexpressing ES cells at day 6 of differentiation supports these findings (not shown). In addition, the reduction of *Dkk-1* mRNA to control levels correlates with the 'shut-off' in MesP1 overexpression caused by silencing of the CMV promoter described above (Supplementary Information, Fig. S1).

On the basis of our results, we suggest that MesP1 has a key role during the earliest time points of cardiovascular determination in the lateral plate mesoderm (Supplementary Information, Fig. S5C). This function seems to be highly conserved among chordates[1,3,7-9]. However, in contrast to our experimental conditions, ectopic heart formation in *Ciona* requires a constitutively active form of Cs-MesP[9]. Aside from MesP1 overexpression, an induction of vertebrate myocardial tissue has only been achieved by overexpression of GATA-5 in Zebrafish[25].

It will therefore be of great interest to identify additional direct target genes of MesP1 and factors regulating MesP1 expression. This knowledge will be required to increase the yield of human cardiovascular cells derived from ES cells for future cell therapy and tissue engineering. It will also be of great interest to transfer this approach to various subpopulations of human adult stem cells, whose cardiac transdifferentiation potential has not yet been proven. Manipulation of these cells by overexpression of MesP1 or other factors may help to overcome the hurdles existing for cardiovascular differentiation of adult stem cells in their native state.

METHODS

Plasmid construction. Human full-length *MesP1* cDNA was amplified from human heart cDNA by proofreading PCR using Pfu-Polymerase (Stratagene) and cloned in pCR-XL-Topo (Invitrogen). Subsequently, the cloned PCR fragment was subcloned into the pIRES-EGFP-2 vector (Clontech) using SacI and PstI. After sequencing, this vector was used for electroporation of GSES cells and subsequent selection of stable clones. pEGFP-N1 served as a control transfection plasmid in non-MesP1-overexpressing cells.

***Xenopus* injections.** *Xenopus* embryos used for *in situ* hybridizations or movie documentations were injected with *MesP1* plasmid DNA (100 pg) at the two-cell stage into one blastomere, according to standard protocols[26]. For these experiments, a Globin 5′UTR cassette[27] had been introduced upstream of the *MesP1* cDNA to stabilize the mRNA in the *Xenopus* embryos. For quantitative RT-PCR, embryos used were injected with either *MesP1* mRNA (4 × 60 pg) or *MesP1* plasmid DNA (4 × 60 pg and 4 × 120 pg).

ES cell culture. Electroporation and isolation of stable clones using the mouse ES cell line GSES were performed according to standard protocols, with minor modifications[28]. Non-linearized vector (5 μg) was used for electroporation (240V/500 μF) of GSES cells (5 × 10^{6}). Transgenic ES cells were grown in high-glucose Dulbecco's modified Eagle medium (DMEM) supplemented with 10% heat-inactivated ES-qualified fetal calf serum (FCS), 2 mM L-glutamine, 50 units ml^{-1} penicillin, 50 μg ml^{-1} streptomycin, 1× non-essential amino acids, 0.4 mg ml^{-1} geneticin (G418) (Gibco), and 0.1 mM β-mercaptoethanol (Sigma). The cells were maintained in an undifferentiated state under feeder-free conditions by addition of 1000 units ml^{-1} purified recombinant mouse LIF (ESGRO, Life Technologies). Cells were maintained at 37 °C in a humidified atmosphere of 5% CO_2/95% air. Monolayers were passaged by trypsinization at confluence (70–80%). For FACS, differentiated cells were dissociated using PBS containing 5 mM EDTA, as described below. *In vitro* differentiation was initiated as follows: GSES cells were collected with 0.25% trypsin-EDTA and dissociated cells were transferred to bacteriological dishes at a density of 2×10^5 ES cells ml^{-1} in Iscove's modified Eagle's medium (IMEM, Sigma) supplemented with 10% heat-inactivated FCS, 2 mM L-glutamine, 50 units ml^{-1} penicillin, 50 μg ml^{-1} streptomycin, 1× non-essential amino acids (Life Technologies) and 450 μM α-monothioglycerol (Sigma). After 2 days, EBs were transferred to new medium. At day 6, EBs of similar size were plated on gelatin-coated tissue culture dishes. The growth medium for the attached differentiation cultures was changed every day.

Western blotting. A peptide antibody specific for amino acids 55–69 of human MesP1 was raised in rabbit and affinity purified. Western blotting was performed according to standard protocols, as previously described[28].

RT-PCR. Semi-quantitative RT-PCR incorporating ^{32}P was performed as described previously[4]. The PCR fragments corresponded to base pairs (bp) 64–189 of *H4*, bp 641–1058 of *GATA4*, bp 1332–1454 of *Nkx2.5*, bp 580–810 of *brachyury*, bp 593–831 of *ANF*, bp 76–226 of *connexin 43*, bp 3–358 of *connexin 45*, bp 1326–1476 of *Mef2c*, bp 5–349 of *TTR*, bp 511–613 of *TnI*, bp 5–260 of *MLC2v*, bp 65–270 of *VE-cadherin*, bp 4–300 of *MyoD*, bp 81–393 of *Neuro D*, bp 315–625 of neurogenin, bp 17–356 of *Cytokeratin 17*, bp 66–386 of *HNF-4*, bp 409–721 of *Oct4*, bp 5–271 of *Nanog*, bp 165–419 of *Rex-1*, bp 50–435 of *Dkk-1* and bp99–478 of *Hex*. The annealing temperature was 57 °C for all primer pairs using 25–32 cycles.

Flow cytometry. For FACS analysis to detect EGFP expression, cells were dissociated in PBS containing 5 mM EDTA for 15 min at 37 °C after washing them twice in PBS without calcium. Subsequently, the cells were centrifuged at 900*g* for 3 min in an Eppendorf centrifuge and resuspended in 100 μl ice-cold PBS containing 2% bovine serum albumin. FACS analysis for EGFP expression was performed immediately after this procedure. For FACS analysis of CD31/PECAM-expressing cells, the protocol included an incubation in PE-conjugated αCD31-antibodies (BD Pharmingen), according to the manufacturer's protocol, before measuring. PE-conjugated IgG_{2a}κ served as isotype controls. FACS analysis for α-actinin was performed as described previously [11], using the primary antibody EA53 (Sigma-Aldrich) and a PE-conjugated secondary antibody (BD Pharmingen). For isotype controls, purified IgG_1κ was used. All FACS analyses for *in vivo* fluorescence as well as surface and intracellular antigens were performed with an Epics XL (Beckman-Coulter) using the evaluation program EXPO32ADC.

Confocal microscopic analysis. Immunostaining was performed according to standard protocols, as described previously[21]. EB outgrowths seeded on 12 mm gelatin-coated glass coverslips were rinsed with PBS fixed for 20 min at room temperature with 3.7% formaldehyde and neutralized with 50 mM glycine. The cells were permeabilized using 0.4% Triton X-100 in PBS and incubated with the primary antibody in a humidified chamber at 37 °C for 2 h. After washing with 0.4% Triton X-100 and PBS, secondary Cy3-conjugated antibody was added and the specimens were incubated for 2 h at 37 °C. Finally, the cells were washed and mounted with Mowiol (Calbiochem).

Electrophysiological analysis. Isolation and electrophysiological analysis of spontaneously beating cardiac cells from EB was performed based on methods described previously[29]. Preparation and analysis of mouse embryonic cardiomyocytes, developmental day 10, was performed as described previously[30]. Please refer to Supplementary Methods for a detailed description.

Electron microscopy. For electron microscopy, the cells were cultivated on gelatine-coated tissue slides until day 12 of differentiation, fixed in 6.25% glutaraldehyde in Soerensen-Phosphate buffer, stained in 2% osmium (in aqua dest. for 1 h), dehydrated in acetone and embedded in epon. By heat-

© 2008 Nature Publishing Group

ing, the polymerized epon plate was snipped off from the tissue slide for cutting ultra thin sections, which were counterstained with uranyl acetate and lead citrate.

ChIP assays. For ChIP assays, transfected cells were fixed in 1% formaldehyde and quenched in 0.125 M glycine. For subsequent cloning of precipitated fragments, further processing was performed as described previously[15]. For PCR (after ChIP assays) primers corresponded to the mouse *Dkk-1* promoter regions (–2.2 kb region: upper primer: 5′-GAATATGGGGAGAGAAGTGG-3′; lower primer: 5′-CAGCATACTACTAGCAATGTC-3′; -3.8 kb Region: upper primer: 5′-GCTTGTCTATCACGATGAGC-3′; lower primer: 5′-GCAAAGATTTCCCGTTCCTG-3′). All ChIP samples were tested for false-positive PCR amplification using primers amplifying 125 bp from the *H4* gene (for genomic DNA contamination).

Electrophoretic mobility shift assays (EMSAs). EMSAs were performed according to the manufacturer's protocol (Pierce) using nuclear extracts from transfected cells. Oligonucleotide sequences used for labelled EMSA probes and 100× specific competition were: mDkk-1 (–3.8 kb): GTCGAGGAGAAAGCATATGCTTTT TATTAAAC; mDkk-1 (–2.2 kb): GAGAGAAGTGGCACATATGTGTATTTC TAGG. For non-specific 100× competition oligonucleotides were: mDkk-1us (–3.8 kb): GTCGAGGAGAAAGaaaATGCTTTTTATTAAAC; mDkk-1us (–2.2 kb): GAGAGAAGTGGCAaaaATGTGTATTTCTAGG. Lower-case letters represent mutations in the bHLH motifs.

Note: Supplementary Information is available on the Nature Cell Biology website.

ACKNOWLEDGEMENTS

We are very grateful for expert technical assistance from Christiane Gross who is funded by the Deutsche Forschungsgemeinschaft (DFG; FR 705/11-3) and the Fritz-Bender-Stiftung. We are also very grateful to Frank Ebel (Max-von-Pettenkofer-Institut, Munich) for helping with the laser scanning microscopy experiments. R.D. is funded exclusively by the DFG (FR 705/11-3). C.B. and F.S. is funded by the FöFoLe program of the LMU Munich. H.L. is supported by an Emmy-Noether Fellowship of the DFG. Additional funding was granted by the Helmut Legalotz-Stiftung for FACS and consumables. We thank Christof Niehrs for the mouse Dkk-1 *in situ* probe and Yumiko Saga for providing us with the MesP1/2 dK.O. embryos.

AUTHOR CONTRIBUTIONS

R. D. designed the experiments together with W.-M. F. and performed promoter studies; J. M.-H. perfromed the electron mcroscoy analyses; R. R., R. D. and E. M. performed the *Xenopus* experiments; R. D. and C. B. performed the molecular cloning and ES cell experiments, and RT-PCR; C. B., F. S. and S. B. performed the FACS and immunostaining; J. S. performed the electrophysiological studies; H. L., M. V. and S. K. performed the wild-type and knockout *in situ* hybridization studies.

Published online at http://www.nature.com/naturecellbiology/
Reprints and permissions information is available online at http://npg.nature.com/reprintsandpermissions/

1. Saga, Y. *et al.* MesP1 is expressed in the heart precursor cells and required for the formation of a single heart tube. *Development* **126,** 3437–3447 (1999).
2. Saga, Y., Kitajima, S. & Miyagawa-Tomita, S. MesP1 expression is the earliest sign of cardiovascular development. *Trends Cardiovasc. Med.* **10,** 345–352 (2000).
3. Kitajima, S., Miyagawa-Tomita, S., Inoue, T., Kanno, J. & Saga, Y. MesP1-nonexpressing cells contribute to the ventricular cardiac conduction system. *Dev. Dyn.* **235,** 395–402. (2006).
4. Maltsev, V. A., Wobus, A. M., Rohwedel, J., Bader, M. & Hescheler, J. Cardiomyocytes differentiated in vitro from embryonic stem cells developmentally express cardiac-specific genes and ionic currents. *Circ. Res.* **75,** 233–244. (1994).
5. Nir, S. G., David, R., Zaruba, M., Franz, W. M. & Itskovitz-Eldor, J. Human embryonic stem cells for cardiovascular repair. *Cardiovasc. Res.* **58,** 313–323 (2003).
6. David, R., Groebner, M. & Franz, W. M. Magnetic cell sorting purification of differentiated embryonic stem cells stably expressing truncated human CD4 as surface marker. *Stem Cells* **23,** 477–482 (2005).
7. Saga, Y. *et al.* MesP1: a novel basic helix-loop-helix protein expressed in the nascent mesodermal cells during mouse gastrulation. *Development* **122,** 2769–2678 (1996).
8. Satou, Y., Imai, K. S. & Satoh, N. The ascidian *MesP* gene specifies heart precursor cells. *Development.* **131,** 2533–2541. (2004).
9. Davidson, B., Shi, W. & Levine, M. Uncoupling heart cell specification and migration in the simple chordate *Ciona intestinalis. Development* **132,** 4811–4818 (2005).
10. Wobus, A. M. *et al.* Retinoic acid accelerates embryonic stem cell-derived cardiac differentiation and enhances development of ventricular cardiomyocytes. *J. Mol. Cell. Cardiol.* **29,** 1525–1539 (1997).
11. Kanno, S. *et al.* Nitric oxide facilitates cardiomyogenesis in mouse embryonic stem cells. *Proc. Natl Acad. Sci. USA* **101,** 12277–12281 (2004).
12. Schroeder, T. *et al.* Recombination signal sequence-binding protein Jκ alters mesodermal cell fate decisions by suppressing cardiomyogenesis. *Proc. Natl Acad. Sci. USA* **100,** 4018–4023 (2003).
13. Tillet, E. *et al.* N-cadherin deficiency impairs pericyte recruitment, and not endothelial differentiation or sprouting, in embryonic stem cell-derived angiogenesis. *Exp. Cell Res.* **310,** 392–400 (2005).
14. Kinder, S. J. *et al.* The organizer of the mouse gastrula is composed of a dynamic population of progenitor cells for the axial mesoderm. *Development* **128,** 3623–3634 (2001).
15. Weinmann, A. S. & Farnham, P. J. Identification of unknown target genes of human transcription factors using chromatin immunoprecipitation. *Methods* **26,** 37–47 (2002).
16. Izumi, N., Era, T., Akimaru, H., Yasunaga, M. & Nishikawa, S. Dissecting the molecular hierarchy for mesendoderm differentiation through a combination of embryonic stem cell culture and RNA interference. *Stem Cells* **25,** 1664–1674 (2007).
17. Sakurai, H. *et al. In vitro* modeling of paraxial and lateral mesoderm differentiation reveals early reversibility. *Stem Cells* **24,** 575–586 (2006).
18. Liu, Y. *et al.* Sox17 is essential for the specification of cardiac mesoderm in embryonic stem cells. *Proc. Natl Acad. Sci. US.* **104,** 3859–3864 (2007).
19. Kitajima, S., Takagi, A., Inoue, T. & Saga, Y. MesP1 and MesP2 are essential for the development of cardiac mesoderm. *Development* **127,** 3215–3226 (2000).
20. Foley, A. C. & Mercola, M. Heart induction by Wnt antagonists depends on the homeodomain transcription factor Hex. *Genes Dev.* **19,** 387–396 (2005).
21. Klaus, A., Saga, Y., Taketo, M. M., Tzahor, E. & Birchmeier, W. Distinct roles of Wnt/β-catenin and Bmp signalling during early cardiogenesis. *Proc. Natl Acad. Sci. USA* **104,** 18531–18536 (2007).
22. Schneider, V. A. & Mercola, M. Wnt antagonism initiates cardiogenesis in *Xenopus laevis. Genes Dev.* **15,** 304–315 (2001).
23. Eisenberg, L. M. & Eisenberg, C. A. Wnt signal transduction and the formation of the myocardium. *Dev. Biol.* **293,** 305–315 (2006).
24. Jaspard, B., Couffinhal, T., Dufourcq, P., Moreau, C. & Duplaa, C. Expression pattern of mouse sFRP-1 and mWnt-8 gene during heart morphogenesis. *Mech. Dev.* **90,** 263–267 (2000).
25. Reiter, J. F. *et al.* Gata5 is required for the development of the heart and endoderm in zebrafish. *Genes Dev.* **13,** 2983–2995 (1999).
26. David, R., Joos, T. O. & Dreyer, C. Anteroposterior patterning and organogenesis of *Xenopus laevis* require a correct dose of germ cell nuclear factor (xGCNF). *Mech. Dev.* **79,** 137–152. (1998).
27. Weintraub, H. *et al.* The *myoD* gene family: nodal point during specification of the muscle cell lineage. *Science* **251,** 761–766 (1991).
28. Muller, M. *et al.* Selection of ventricular-like cardiomyocytes from ES cells *in vitro. Faseb J.* **14,** 2540–2548 (2000).
29. Stieber, J. *et al.* The hyperpolarization-activated channel HCN4 is required for the generation of pacemaker action potentials in the embryonic heart. *Proc. Natl Acad. Sci. USA* **100,** 15235–15240 (2003).

© 2008 Nature Publishing Group

J Membrane Biol (2007) 217:105–113
DOI 10.1007/s00232-007-9042-z

Membrane Channel Connexin 32 Maintains Lin$^-$/c-kit$^+$ Hematopoietic Progenitor Cell Compartment: Analysis of the Cell Cycle

Yoko Hirabayashi · Byung-Il Yoon · Isao Tsuboi · Yan Huo · Yukio Kodama · Jun Kanno · Thomas Ott · James E. Trosko · Tohru Inoue

Received: 30 April 2007 / Accepted: 14 May 2007 / Published online: 15 July 2007
© Springer Science+Business Media, LLC 2007

Abstract Membrane channel connexin (Cx) forms gap junctions that are implicated in the homeostatic regulation of multicellular systems; thus, hematopoietic cells were assumed not to express Cxs. However, hematopoietic progenitors organize a multicellular system during the primitive stage; thus, the aim of the present study was to determine whether Cx32, a member of the Cx family, may function during the primitive steady-state hematopoiesis in the bone marrow (BM). First, the numbers of mononuclear cells in the peripheral blood and various hematopoietic progenitor compartments in the BM decreased in Cx32-knockout (KO) mice. Second, on the contrary, the number of primitive hematopoietic progenitor cells, specifically the Lin$^-$/c-kit$^+$/Scal$^+$ fraction, the KSL progenitor cell compartment, also increased in Cx32-KO mice. Third, expression of Cx32 was detected in Lin$^-$/c-kit$^+$ hematopoietic progenitor cells of wild-type mice (0.27% in the BM), whereas it was not detected in unfractionated wild-type BM cells. Furthermore, cell-cycle analysis of the fractionated KSL compartment from Cx32-KO BM showed a higher ratio in the G_2/M fraction. Taken together, all these results imply that Cx32 is expressed solely in the primitive stem cell compartment, which maintains the stemness of the cells, i.e., being quiescent and noncycling; and once Cx32 is knocked out, these progenitor cells are expected to enter the cell cycle, followed by proliferation and differentiation for maintaining the number of peripheral blood cells.

Keywords Connexin 32 · Hematopoiesis · Hematopoietic stem cell · Cx32-knockout mouse

Y. Hirabayashi (✉) · B.-I. Yoon · I. Tsuboi ·
Y. Huo · Y. Kodama · J. Kanno
Division of Cellular and Molecular Toxicology, Center for Biological Safety and Research, National Institute of Health Sciences, 1-18-1 Kamiyohga, SetagayakuTokyo 158-8501, Japan
e-mail: yokohira@nihs.go.jp

B.-I. Yoon
Laboratory of Histology and Molecular Pathogenesis, School of Veterinary Medicine, Kangwon National University, Chuncheon 200-701, Republic of Korea

T. Ott
Service Einrichtung Transgene Tiere, Hertie-Institut für Klinische Hirnforschung, Tübingen 72076, Germany

J. E. Trosko
Department of Pediatrics and Human Development, Michigan State University, College of Human Medicine, East Lansing, MI 48824, USA

T. Inoue
Center for Biological Safety and Research, National Institute of Health Sciences, Tokyo 158-8501, Japan

Introduction

Connexin (Cx) functions in the organization of cell-cell communication via gap junctions in multicellular organisms. Gap junctions have been implicated in the homeostatic regulation of various cellular functions, including growth control and differentiation (Loewenstein, 1979), apoptosis (Wilson, Close & Trosko, 2000) and the synchronization of electrotonic and metabolic functions (Bruzzone, White & Paul, 1996).

The role of Cxs in hematopoietic organs is poorly understood, except that the expression of Cx43 between hematopoietic progenitor cells and bone marrow (BM) stromal cells sustains hematopoiesis (Rosendaal, Gregan & Green, 1991; Ploemacher et al., 2000; Cancelas et al.,

2000; Montecino-Rodriguez, Leathers & Dorshkind, 2000). As Cxs are essential molecules for multicellular organisms, Cxs that organize cell-cell communication within the hematopoietic progenitor cell compartment are surmised to be present in BM tissue. If Cxs are present among hematopoietic progenitor cells, what would be their functions?

Krenacs & Rosendaal (1998) previously reported that Cx32 is not expressed in the BM. Therefore, if Cx32 is expressed in the blood cells, such Cx32-expressing cells would likely be, e.g., solely hematopoietic stem/progenitor cells. Such a specific study was supposed to be supported by the use of knockout (KO) mice for specific Cx molecules. Consequently, we found a functional impairment of the BM in Cx32-KO mice in our benzene exposure experiment (Yoon et al., 2004).

Cx32-KO mice were first established in 1996 by Willecke (Nelles et al., 1996). Using these Cx32-KO mice, an analysis of the possible functions of Cx32 in hematopoietic stem/progenitor cells was conducted using a reverse biological approach. Cx32-KO mice showed decreased numbers of peripheral mononuclear cells, various progenitor cell compartments and an increased primitive stem cell fraction, such as the lineage marker-negative (Lin^-)/c-kit-positive ($c\text{-}kit^+$)/stem cell antigen-1-positive ($Sca1^+$) (=KSL) fraction. On the contrary, in wild-type mice, expression of Cx32 was detected by immunocytochemistry and reverse transcriptase-polymerase chain reaction (RT-PCR), although it was not detected in unfractionated wild-type BM cells. Subsequent cell-cycle analyses, one for colony-forming progenitors using the method for evaluation of cycling progenitor cells with incorporation of bromodeoxyuridine (BrdUrd) followed by exposure to ultraviolet A (UVA) (see, BUUV Assay in Materials and Methods) and the other using a cell sorter with Hoechst 33342 for the KSL fraction, showed a significant increase in the ratio of the cell-cycle fraction in both compartments in the BM of Cx32-KO mice. The functions of Cx32, which is expressed in primitive hematopoietic stem/progenitor cells, are likely restoration of stem/progenitor cell quiescence and maintenance of primitive stem cells to prevent exhaustion.

Materials and Methods

Experimental Animals

Cx32-KO mice ($Cx32^{-/-}$ or $Cx32^{-/Y}$) were genetically modified from the F_1 embryonic cell line 129/J and the C57BL/6 strain developed by Willecke (Nelles et al., 1996). Heterozygous mice ($Cx32^{-/+}$) backcrossed with the C57BL/6 strain and maintained at the animal facility of the National Institute of Health Sciences (NIHS), Tokyo, Japan, were used. The pups were genotyped by PCR for screening of DNA from their tails.

Eight-week-old C57BL/6 male mice from Japan SLC (Hamamatsu, Japan) were used for the colonization assay. All experimental protocols involving laboratory mice in this study were reviewed by a peer review panel, the Interdisciplinary Monitoring Committee for the Right Use and Welfare of Experimental Animals, established at the NIHS, and approved by the Committee for Animal Care and Use at the NIHS with the experimental code 224-37009639415-2002.

Blood and BM Separation

The numbers of peripheral white blood cells, platelets and red blood cells were measured using a Coulter counter (Sysmex K-4500; Sysmex, Kobe, Japan). BM cells were harvested from the femur of each mouse (Yoon et al., 2001) after the animals were killed by cervical dislocation under deep anesthesia with ethyl ether. A 26-gauge needle was inserted into the femoral bone cavity through the proximal and distal ends of the bone shafts, and BM cells were flushed out under pressure by injecting 2 ml of α-minimum essential medium (α-MEM) with ribonucleosides and deoxyribonucleosides (Invitrogen, Carlsbad, CA).

Antibodies and Immunomagnetic Bead Separation

For the depletion of differentiated (lineage marker-positive) cells from BM cells, immunomagnetic bead separation (BD IMag Mouse Hematopoietic Progenitor Cell Enrichment™ set; BD Biosciences, San Jose, CA) or immunobead density gradient separation (SpinSep™; StemCell Technologies, Vancouver, Canada) was performed. As for lineage (Lin) markers, a biotinylated antibody cocktail (BD Biosciences) containing anti-mouse CD3e (145-2C11), CD11b (M1/70), CD45R/B220 (RA3-6B2), Ly-6G and Ly-6C/Gr-1 (RB6-8C5) and TER-119/erythroid cell (TER-119) antibodies and a monoclonal antibody cocktail (SpinSep) containing anti-CD5/Ly-1, CD45R, CD11b/Mac-1, Ly-6G/Gr-1, TER119 and 7/4/neutrophil antibodies were used. As a secondary antibody for the former biotinylated antibody cocktail, streptavidin (StAv)-coated beads (BD Biosciences) for depletion and StAv-peridinin chlorophyll-a protein (PerCP, BD Biosciences) for visualization were used. For the latter cocktail (SpinSep), an optimized combination antibody cocktail against it that had been coated on dense microparticles, i.e., SpinSep Mouse Dense Particles (StemCell Technologies), was used for immunoprecipitation.

For enrichment of the $c\text{-}kit^+$ fraction by immunomagnetic bead separation, CD117/c-kit-conjugated phycoerythrin (PE, StemCell Technologies) was used as a progenitor

marker and, as a secondary antibody, an anti-PE tetrameric antibody complex (StemCell Technologies) was used.

For detection of Cx32-positive cells by flow cytometry, a mouse anti-Cx32 monoclonal antibody from two sources (Chemicon International, Temecula, CA; Santa Cruz Technology, Santa Cruz, CA) as a primary antibody and an anti-mouse immunoglobulin (Ig) conjugated with fluorescein isothiocyanate (FITC) as a secondary antibody (BD Biosciences) were used.

For cell-cycle analysis by flow cytometry, as lineage markers, the same antibody cocktails from BD Biosciences were used. In addition, CD117/c-kit conjugated with allophycocyanin (APC), stem cell antigen (Sca1) antibody conjugated with PE and an AT-rich DNA-binding dye, Hoechst 33342 (Sigma, St. Louis, MO), were used.

Immunohistochemical Analysis

The same anti-Cx32 antibody (Chemicon International) was used as the primary antibody. As for the secondary antibody, a biotinylated horse anti-mouse Ig G (Vector Laboratories, Burlingame, CA) was used, and streptavidin labeled with peroxidase and 3,3′-diaminobenzidine was used to detect immunoreactivity (Vector Laboratories).

Enrichment of BM Cells in $Lin^-/c\text{-}kit^+$ Fraction

The $Lin^-/c\text{-}kit^+$ fraction is rich in hematopoietic stem cells (HSCs). To obtain a large number of $Lin^-/c\text{-}kit^+$ progenitor cell-enriched fraction in BM cells, a combination of immunobead density gradient and immunomagnetic bead separation techniques was carried out. First, for the depletion of lineage-positive BM cells, harvested BM cells were processed through an immunobead density gradient using a density-matched medium and dense microparticles coated with a cocktail of an optimized combination of antibodies called SpinSep (StemCell Technologies). Second, for the selection of the $c\text{-}kit^+$ fraction, immunomagnetic bead separation using magnetic nanoparticles with a magnetic holder was carried out according to the manufacturer's instruction (StemCell Technologies). For each procedure, the antibodies used are described under Antibodies and Immunomagnetic Bead Separation, above.

Flow-Cytometric Analysis using Anti-Cx32 Antibody

BM cells with or without fractionation for $Lin^-/c\text{-}kit^+$ HSC enrichment were stained with the biotinylated antibody cocktail of StAv-PerCP, c-kit-PE, the anti-Cx32 antibody and anti-mouse IgG conjugated with FITC. Flow-cytometric analysis was carried out using FACSVantage and FACSAria (both from BD Biosciences).

Flow-Cytometric Analysis for Cell Cycle of KSL Fraction

Lineage-depleted BM cells were stained with the biotinylated antibody cocktail with StAv-PerCP, c-kit-APC, Sca1-PE and Hoechst 33342. Flow-cytometric analysis was carried out using FACSAria.

BUUV Assay

Hematopoietic progenitor cell-specific kinetic studies were evaluated by continuous labeling by an osmotic minipump (Alza, Palo Alto, CA) of BrdUrd for cycling cells, followed by UVA exposure and hematopoietic colonization assay (BUUV assay, details in Hirabayashi et al., 1998, 2002).

Irradiation

In the assay of hematopoietic progenitor cells, recipient mice were exposed to a lethal radiation dose of 915 cGy, at a dose rate of 124 cGy per minute, using a ^{137}Cs-gamma irradiator (Gammacell 40 Exactor; MDS Nordin, Ottawa, Canada) with a 0.5-mm aluminum-copper filter.

Assay for Colony-Forming Units in Spleen

The Till & McCulloch (1961) method was used to determine the number of hematopoietic spleen colonies, i.e., colony-forming units in spleen (CFU-S), formed by hematopoietic progenitor cells. Aliquots of a BM cell suspension were used for evaluating the numbers of CFU-S. Spleens were harvested 9 or 13 days after BM transplantation for determining the number of CFU-S-9 or CFU-S-13 and then fixed in Bouin's solution. Macroscopic spleen colonies were counted under an inverted microscope at ×5.6. It was previously shown, using the C57BL/6 strain, that all colonies visible on days 9 and 13 originate from transplanted BM cells under the condition that the recipient mice are exposed to a lethal radiation dose of 915 cGy (Hirabayashi et al., 2002).

Assay for Granulocyte-Macrophage Colony-Forming Units

Granulocyte-macrophage colony-forming units (CFU-GM) were assayed in semisolid methylcellulose culture (Yoon et al., 2001; Hirabayashi et al., 2002). Briefly, 8×10^4 BM cells suspended in 100 μl of α-MEM were added to 3.9 ml of culture medium containing 1% methylcellulose (Nakarai-Tesque, Kyoto, Japan), 30% fetal calf serum (HyClone Laboratories, Logan, UT), 1% bovine serum albumin (Sigma), 10^{-4} M mercaptoethanol (Sigma) and 10 ng/ml murine granulocyte-macrophage